energies

MDPI

Article

Applying Reservoir Simulation and Artificial Intelligence Algorithms to Optimize Fracture Characterization and CO_2 Enhanced Oil Recovery in Unconventional Reservoirs: A Case Study in the Wolfcamp Formation

Xincheng Wan [1,2,*], Lu Jin [1,2], Nicholas A. Azzolina [1,2], Shane K. Butler [1,2], Xue Yu [1,2] and Jin Zhao [1,2]

[1] National Energy Technology Laboratory, Department of Energy, Morgantown, WV 26505, USA
[2] Energy & Environmental Research Center, University of North Dakota, Grand Forks, ND 58202, USA
* Correspondence: xwan@undeerc.org

Abstract: Reservoir simulation for unconventional reservoirs requires proper history matching (HM) to quantify the uncertainties of fracture properties and proper modeling methods to address complex fracture geometry. An integrated method, namely embedded discrete fracture model–artificial intelligence–automatic HM (EDFM–AI–AHM), was used to automatically generate HM solutions for a multistage hydraulic fracturing well in the Wolfcamp Formation. Thirteen scenarios with different combinations of matrix and fracture parameters as variables or fixed inputs were designed to generate 1300 reservoir simulations via EDFM–AI–AHM, from which 358 HM solutions were retained to reproduce production history and quantify the uncertainties of matrix and hydraulic fracture properties. The best HM solution was used for production forecasting and carbon dioxide (CO_2)-enhanced oil recovery (EOR) strategy optimization. The results of the production forecast for primary recovery indicated that the drainage area for oil production was difficult to extend further into the low-permeability reservoir matrix. However, CO_2 EOR simulations showed that increasing the gas injection rate during the injection cycle promoted incremental oil production from the reservoir matrix, regardless of minimum miscibility pressure. A gas injection rate of 25 million standard cubic feet per day (MMscfd) resulted in a 14% incremental oil production improvement compared to the baseline scenario with no EOR. This paper demonstrates the utility of coupling reservoir simulation with artificial intelligence algorithms to generate ensembles of simulation cases that provide insights into the relationships between fracture network properties and production.

Keywords: CO_2 EOR; reservoir simulation; artificial intelligence; unconventional reservoir; fracture characterization

check for updates

Citation: Wan, X.; Jin, L.; Azzolina, N.A.; Butler, S.K.; Yu, X.; Zhao, J. Applying Reservoir Simulation and Artificial Intelligence Algorithms to Optimize Fracture Characterization and CO_2 Enhanced Oil Recovery in Unconventional Reservoirs: A Case Study in the Wolfcamp Formation. *Energies* **2022**, *15*, 8266. https://doi.org/10.3390/en15218266

Academic Editor: Reza Rezaee

Received: 12 October 2022
Accepted: 2 November 2022
Published: 4 November 2022

Publisher's Note: MDPI stays neutral with regard to jurisdictional claims in published maps and institutional affiliations.

Copyright: © 2022 by the authors. Licensee MDPI, Basel, Switzerland. This article is an open access article distributed under the terms and conditions of the Creative Commons Attribution (CC BY) license (https://creativecommons.org/licenses/by/4.0/).

1. Introduction

Reservoir simulation plays an important role in the evaluation, optimization, and management of unconventional reservoirs because of the complex fluid flow behavior in the low-permeability matrix (nano- to micro-Darcy range) and the complex fracture network comprising natural and hydraulic (stimulated) fractures. The presence of natural and hydraulic fractures creates challenges for an effective simulation study when a detailed sensitivity analysis is required to investigate the effect of fracture network properties on production. For conventional reservoir simulation, reservoir properties such as reservoir permeability and porosity can be obtained from well log and core data. However, for unconventional reservoir simulation, the fracture network geometry is highly uncertain and difficult to observe or measure. A diagnostic fracture injection test (DFIT) can provide fracture geometry information, but the interpretation is limited by data obtained over a short period [1]. Microseismic is another approach to characterize fracture geometry; however, the fracture geometry described by microseismic is stimulated reservoir volume

(SRV), which is larger than the effective fracture geometry that contributes to production [2]. In addition, the fracture conductivity, or the ability of the fracture network to transmit fluids, cannot be obtained from microseismic interpretation. Reservoir simulation provides a quantitative method for evaluating the effect of the fracture network properties on production when the geometry and conductivity of the fracture network are uncertain. There are two critical aspects for properly characterizing the fracture network that contributes to production. First, proper history matching (HM) is needed to identify the fracture network properties that yield the closest match between simulated and observed production history. Second, the fractures need to be efficiently embedded in the simulation model to ensure that the simulation model can run smoothly over multiple cases.

1.1. Automatic History Matching

HM is an inverse problem that uses observed production behavior to evaluate the reservoir matrix and fracture properties [3]. One of the challenges with HM is that multiple combinations of reservoir matrix and fracture properties may provide sufficient HM results. Therefore, a single HM solution may not correctly describe reservoir conditions and fracture properties. Instead, an ensemble of solutions should be evaluated for better assessment of the reservoir matrix and fracture network uncertainties and better predictions of future production. Manual HM requires sound engineering judgment, and the process is labor- and time-intensive. To efficiently generate multiple HM solutions for better characterization of the reservoir and fractures, automatic history matching (AHM) is needed. In this context, AHM refers to a process where computer codes and algorithms sample a user-defined parameter space for the matrix and fracture network properties, execute reservoir simulations with the parameter values, and repeat the process until the iterations converge towards the best estimates for the matrix and fracture network properties.

The key to AHM is the algorithm for uncertainty characterization. The Markov chain Monte Carlo (MCMC) method is one of the most effective sampling methods for uncertainty characterization and HM; however, performing MCMC for AHM is time-consuming because it requires the realization of multiple reservoir models that are computationally expensive and require many hours to run one simulation case depending on the computing power [3–5]. The randomized maximum likelihood (RML) method has been demonstrated to generate acceptable uncertainty quantification results for some HM problems with less computational effort than MCMC [5,6]. However, the posterior samples provided by the RML method could be biased for some nonlinear relationships between reservoir model variables and production data, leading to unsuccessful HM performance [7,8]. The ensemble Kalman filter (EnKF) has been proven to be efficient and flexible for uncertainty quantification; however, EnKF fails to provide reasonable quantification of uncertainties for strongly nonlinear problems [5,7]. To improve the computational efficiency while maintaining the accuracy of uncertainty quantification, a workflow was proposed to replace the reservoir simulator with proxy models obtained from artificial neural networks (ANNs), one of several types of artificial intelligence (AI) or machine learning (ML) algorithms widely used for complex input–output relationships between features and target variables [9]. The proposed procedure significantly reduces the computational effort and makes the application of MCMC sampling in HM feasible. Tripoppoom et al. improved the original ANN–MCMC workflow by replacing a single proxy model with multiple proxy models for MCMC sampling to minimize the nonlinearity of the HM [10]. The multiple proxy-based MCMC approach with neural networks (NNs) as the proxy models was chosen in this study to perform AHM (hereafter NN–MCMC).

1.2. Embedded Discrete Fracture Model

To successfully perform an automatic history matching (AHM) procedure for unconventional reservoirs, it is crucial to model multistage hydraulic fractures and complex natural fracture geometry. A conventional method to include fractures in a reservoir model is the dual-porosity, dual-permeability (DP/DK) approach. The DP/DK approach is effi-

cient in providing solutions for models of small scale or with uniformly distributed natural fractures, but the accuracy is low for modeling fractures with irregular geometry and high heterogeneity [11–13]. Local grid refinement (LGR) and unstructured grid (UG) methods provide higher accuracy for simulating complex fracture geometry; however, they require longer computational time because a heavy and complicated gridding structure is needed for modeling fractures [14–16]. The embedded discrete fracture model (EDFM) method combines the advantages of DP/DK, LGR, and UG methods. The accuracy of the EDFM method is comparable to the LGR and UG methods, but the EDFM method requires less computing time. The EDFM method was adopted in this study to construct fractures that were then integrated into a compositional reservoir simulation model for flow simulation.

1.3. Production Forecast

After better understanding matrix and fracture properties and obtaining the optimum reservoir model via the AHM workflow, the simulation model can be used for production forecasts (predictions of future oil, gas, and water production) and the optimization of well operations or sets of well operations.

1.4. Study Goal and Objectives

The goal of this study was to illustrate a workflow for applying the NN–MCMC approach and the EDFM method to characterize the matrix and fracture network properties in an unconventional reservoir and generate production forecasts. The study design included the following objectives: (i) select a test site for an unconventional reservoir, (ii) develop a reservoir simulation model for a representative well from the test site, (iii) apply the EDFM method to describe the fracture network around the selected well, (iv) implement the NN–MCMC approach to generate an ensemble of simulation cases for the test well and to match historical (observed) production, and (v) generate production forecasts to estimate primary recovery oil production and to explore different strategies for enhanced oil recovery (EOR) with carbon dioxide (CO_2) injection.

2. Test Site Description

2.1. Reservoir Overview

The test site studied in this work is a hydraulic fracturing test site, HFTS-1-Midland, located in the Wolfcamp Formation of the Midland Basin in Reagan County, Texas. The Midland Basin is part of the Permian Basin, which is one of the largest oil and gas production basins in the United States. In 2021, the Permian Basin contributed to 42% of crude oil production and more than 20% of natural gas production in the United States [17]. As of 2016, the technically recoverable oil, gas, and natural gas liquid (NGL) of the Wolfcamp Formation in the Midland Basin were 20 billion barrels, 16 trillion cubic feet, and 1.6 billion barrels, respectively, making the Midland Basin one of the largest hydrocarbon plays in the United States [18].

The Wolfcamp Formation in the Midland Basin consists of carbonate, evaporite, siliciclastic materials, lime mudstone, and dark shale [19,20]. Large amounts of organic materials that were accumulated in the Midland Basin during the early sedimentation period were later converted to oil and gas. Core sample analysis indicates that the Wolfcamp Formation in the Midland Basin has total organic carbon (TOC) of up to 8.7%, indicating high potential for oil and gas generation [21,22].

2.2. Production Overview

The HFTS-1-Midland site consists of 11 wells: 3SU, 4SM, 4SU, 5SM, 5SU, 6SM, 6SM, 7SM, 7SU, 8SM, and 8SU, as shown in Figure 1. The suffixes “SM” and “SU” refer to wells completed in the Middle Wolfcamp and the Upper Wolfcamp, respectively. The well spacing is approximately 660 feet within the same layer, and the range of lateral offset between two adjacent “SM” and “SU” wells is from 290 to 370 feet [23]. The wells are located at a depth of approximately 7700 feet. A review of the production history

of the 11 wells revealed similar trends in oil, water, and gas production within the same production period. Well 7SU was selected as the candidate for reservoir simulation to investigate the production dynamics of the site and to develop the reservoir simulation model and EDFM fracture network.

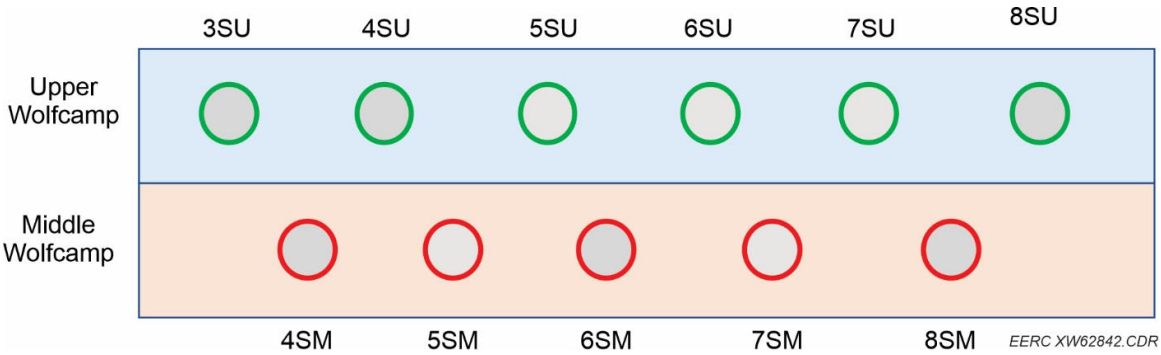


Figure 1. Profile view of the HFTS-1-Midland site Upper and Middle Wolfcamp wells.

2.3. HFTS Data Analysis

Through research conducted at HFTS-1-Midland (separate from the current study), extensive data were acquired from the Middle and Upper Wolfcamp Formations at the test site to characterize fracture geometry, identify interwell interference, analyze pressure response, and evaluate production performance [24]. Downhole microseismic mapping (MSM) data were obtained from approximately 434 fracturing stages. The MSM data suggest that the fracture geometry is relatively consistent for all the wells, and most of the hydraulic fractures appear to have relatively symmetric fracture growth in fracture length [25]. The core and image logs show that natural fractures exist in the test site, but more than 70% of the natural fractures are sealed, and the remaining natural fractures are possibly induced during hydraulic fracturing, drilling, or core handling [26]. These observations imply that while a few non-sealed natural fractures provide an insignificant amount of hydrocarbon production, the induced hydraulic fractures contribute to most of the hydrocarbon production. Based on these observations, the modeling and characterization of hydraulic fractures constitute the primary focus of this study.

High-frequency bottomhole pressure (BHP) data were collected via two pressure interference tests (PITs) performed at 7 and 18 months of production time to identify interwell communication between the active and observation wells [23]. Before well 4SU's shut-in at the time of $t = 25.9$ h , the pressure buildup of Well 3SU follows a power law trend baseline. After Well 4SU's shut-in, the pressure buildup of Well 3SU deviates from the power law trend baseline [23]. The pressure deviation ΔP between the buildup pressure and power law trend line is used to calculate Chow Pressure Group (CPG), which is defined as:

$$CPG = \frac{\Delta P}{2(\Delta P')} \tag{1}$$

and $\Delta P'$ is the natural logarithmic derivative of ΔP calculated by:

$$\Delta P' = \frac{d(\Delta P)}{d(\ln(\Delta t))} \tag{2}$$

where Δt is the time difference between the actual time and the shut-in time of Well 4SU [27,28]. The curves of ΔP, $\Delta P\prime$, and CPG against Δt are presented on a log–log plot (Figure 2) to quantify the magnitude of pressure interference (MPI). The MPI value of 0.625 is obtained by reading the stabilized CPG value (the blue solid diamonds show straight-line character) for the interference of Well 4SU shut-in on Well 3SU in Figure 2. This same approach is applied to estimate MPI values between other wells, as shown in Figure 3. The

MPIs have ranges from 0 to 1. Higher MPI values indicate strong pressure interference caused by interwell fracture connection.

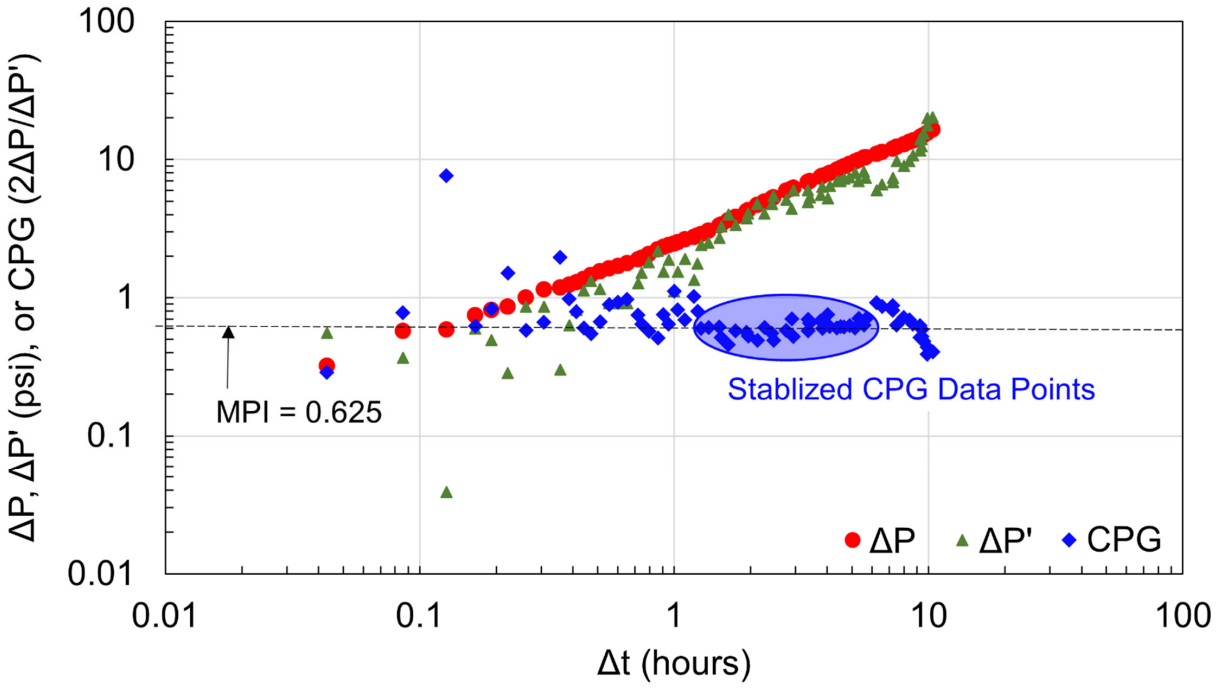


Figure 2. MPI estimated from the stabilized CPG: red solid circle represents the pressure difference ΔP between pressure build-up of Wwell 3SU and the predicted power law trend line at time Δt after shut-in of Well 4SU; green solid triangle represents the derivative of ΔP at time Δt; blue solid diamond represents the *CPG* at time Δt (modified from [23]).

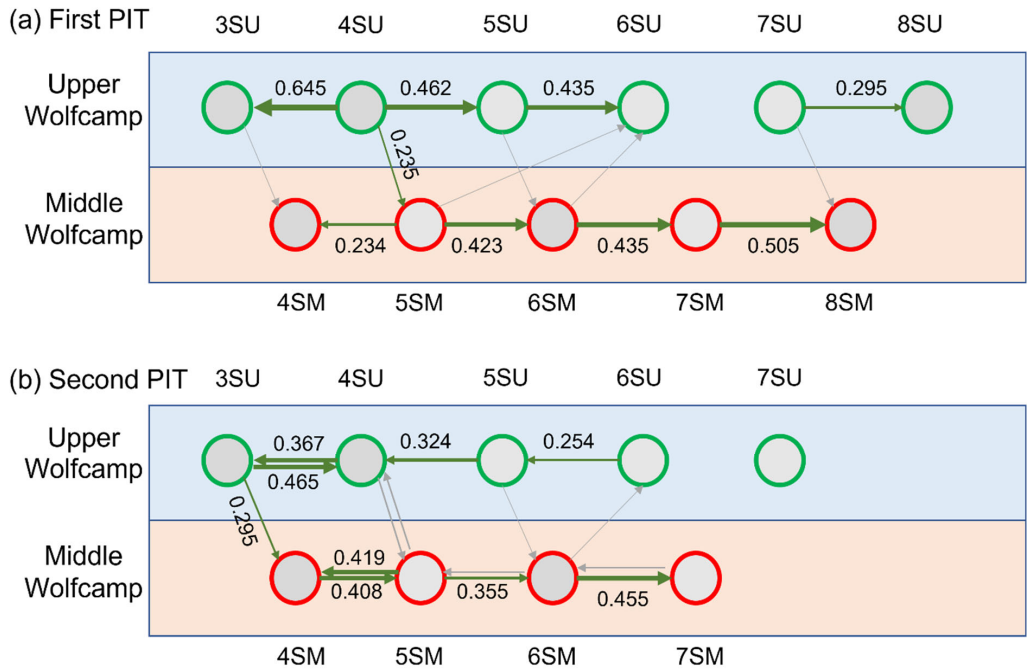


Figure 3. Pressure interference detected during the first (**a**) and second (**b**) pressure interference tests (PITs) at the HFTS-1-Midland site. Green arrows with MPI values on the side show measurable pressure interference. Gray arrows represent non-measurable pressure interference. The direction of all the arrows is from the monitored well to the observation well. The second PIT results for Wells 8SU and 8SM were missing (modified from [23]).

Comparing Figure 3a,b, the MPIs among the Upper Wolfcamp wells decreased from the first to second pressure interference test (PIT), while the change in MPIs among the Middle Wolfcamp wells was not significant. The results imply that the fractures connecting the Upper Wolfcamp wells were closing from the first to second PIT, while the fracture closure effect was not significant for the Middle Wolfcamp wells from the first to 2 s PIT. The PIT results also show that the pressure interference from other wells to Well 7SU is the smallest because no arrow points to Well 7SU. Despite the pressure data for Wells 8SU and 8SM being lost for the second PIT, the information provided in Figure 3a and the fracture closure effect together imply that the pressure interference from other wells to Well 7SU during the second PIT was not significant.

3. Reservoir Simulation Model Development

3.1. Equation of State (EOS) Modeling

Crude oil collected from Well 6SU was used to measure pressure, volume, and temperature (PVT) data. The oil was relatively light, as 82.9 mol % of the components were hydrocarbons below decane (C10) and 53.2 mol % of the components were gas components, including C1 (methane), C2 (ethane), and C3 (propane), as shown in Figure 4.

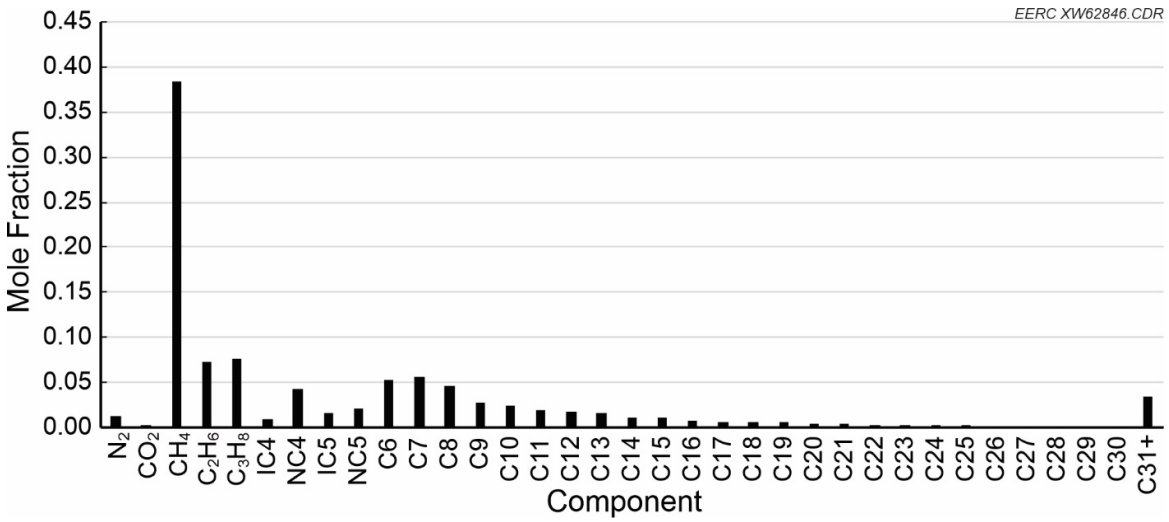


Figure 4. Composition of the Upper Wolfcamp oil acquired from Well 6SU used for EOS modeling. "IC" refers to iso-alkanes, with C equal to the carbon number. "NC" refers to normal alkanes. "C" with no "I" or "N" prefix refers to either iso- or normal alkanes within the specific carbon number range.

A series of pressure–volume–temperature (PVT) experiments including separator test, constant composition expansion (CCE) test, and differential liberation (DL) test were performed to measure the phase behavior of the crude oil in a wide range of pressure and temperature conditions. Based on the experimental data, an equation of state (EOS) was regressed using the Peng–Robinson method. Table 1 shows the ten components used in the regressed EOS, which satisfactorily matched the experimental data, as illustrated in Figure 5. The EOS was integrated into the geologic model for dynamic reservoir simulation.

3.2. EDFM Method

The recently developed nonintrusive EDFM method allows complex fracture geometry to be simulated via structured grids; thus, the obtained complex fracture geometry can be integrated into a regular compositional reservoir model to perform simulation for unconventional reservoirs [29,30]. The EDFM method assists reservoir simulation via inserting fracture cells into the reservoir model using the non-neighboring connection (NNC) approach [29–31].

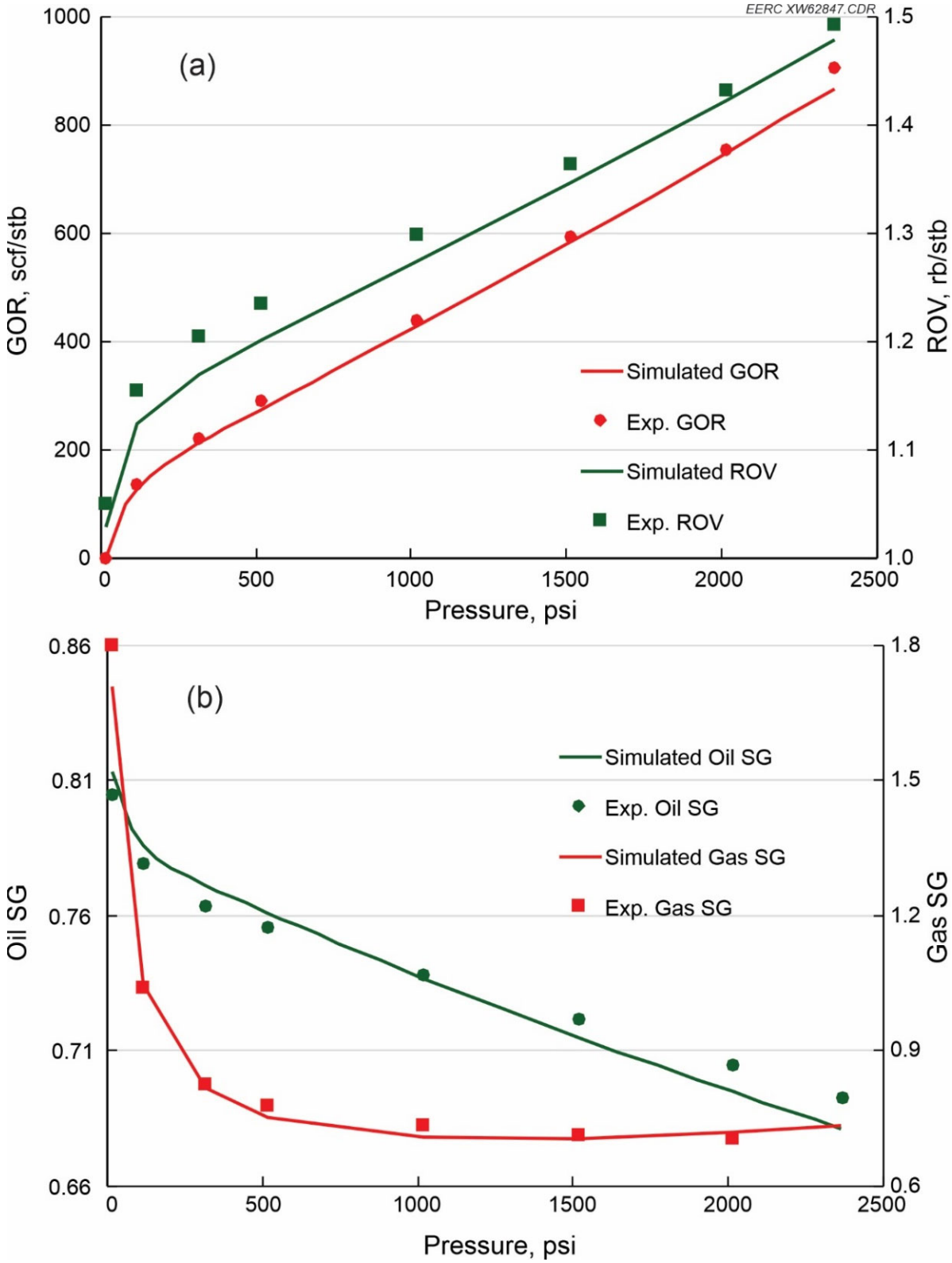


Figure 5. Simulated data (green or red lines) and experimental data (green or red symbols) comparisons for the 10-component EOS model: (**a**) gas/oil ratio (GOR) and relative oil volume (ROV) and (**b**) oil and gas specific gravity (SG). Gas SG is the ratio of the density of the gas to the density of air at 1 atm pressure at 60 °F. Oil SG is the ratio of the oil's density to that of water at 60 °F.

Table 1. Components and mole fractions of the EOS model.

Index	Component Name	Mole Fraction, %
1	N_2	1.19
2	CO_2	0.24
3	CH_4	38.34
4	C_2H_6	7.26
5	C_3H_8	7.62
6	IC4 to NC4	5.19
7	IC5 to C7	13.99
8	C8 to C12	11.03
9	C13 to C19	7.05
10	C20 to C31+	8.09

"IC" refers to iso-alkanes, with C equal to the carbon number. "NC" refers to normal alkanes. "C" with no "I" or "N" prefix refers to either iso- or normal alkanes within the specific carbon number range.

Three types of non-neighboring connections (NNCs) are: (i) NNC Type I—matrix and fracture connection, (ii) NNC Type II—fracture segments connection in a single fracture, and (iii) NNC Type III—a connection between two intersecting fracture segments. If a new fracture segment is added to the physical domain, then a non-neighboring new fracture cell will be added to the computational domain accordingly to calculate fluid flow inside fractures or between fractures and the rock matrix. The NNC approach allows the simulation of three-dimensional (3D) nonplanar and slanted fractures using additional two-dimensional (2D) fracture cells. Therefore, the EDFM method can maintain simulation accuracy while significantly improving computational efficiency [29–34].

3.3. Description of Reservoir Simulation Model

The goal of this study was to illustrate a workflow for applying the NN–MCMC approach and the EDFM method to characterize the matrix and fracture network properties and not to match production for all 11 HFTS-1-Midland wells. Thus, a single-well reservoir simulation model for Well 7SU was built using the reservoir parameters, the EOS model, and fractures created using EDFM. Figure 6 shows an oblique view of the reservoir simulation model with horizontal wellbore and hydraulic fractures, and Table 2 shows the basic reservoir, wellbore, and fracturing data for the simulated Well 7SU. Natural fractures were not simulated in this study because of a lack of available data and observations by other HFTS-1-Midland researchers that natural fractures minimally contribute to the fracture network fluid flow as compared to hydraulic fractures [25]. The grid size of the model was 41 ft in both X- and Y-directions. The grid size varied from 26.4 to 118.7 ft/cell in the Z-direction to represent the different thicknesses of layers in the vertical direction. The purpose was to refine the region containing Well 7SU and its hydraulic fractures so the fracture–matrix and matrix–matrix flow calculations could be more accurate. The number of grids in the X-, Y-, and Z-directions was 274, 34, and 16, respectively. The length (in the Y-direction), width (in the X-direction), and height (in the Z-direction) of the model were 11,234 ft, 1394 ft, and 802 ft, respectively. An additional four grids were added to the X-direction to represent non-neighboring hydraulic fractures. The added grids were only used for flow calculation without impacting the material balance in the model.

3.4. Manual History Matching (HM) Results

Prior to running the automatic history matching (AHM), a manual HM was performed to evaluate the reservoir simulation response against measured BHP, oil rate, and water rate for Well 7SU. For all the HM results presented in Figure 7, the field and simulation data were normalized upon operator request [35]. The oil and water rate data were normalized by dividing the data value by the field maximum oil rate. The well BHP data were normalized by dividing the data value by the initial reservoir pressure.

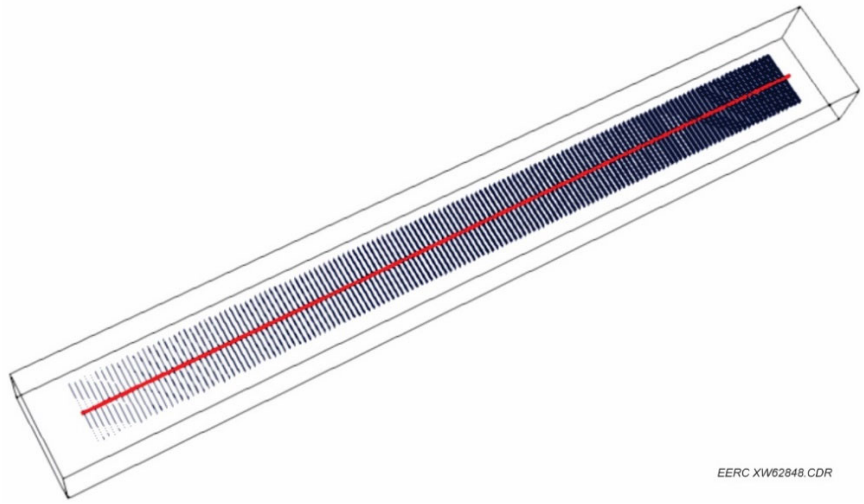


Figure 6. Oblique view of the reservoir simulation model with hydraulic fractures. The red line is Well 7SU, and the blue hatching denotes the EDFM fracture grids.

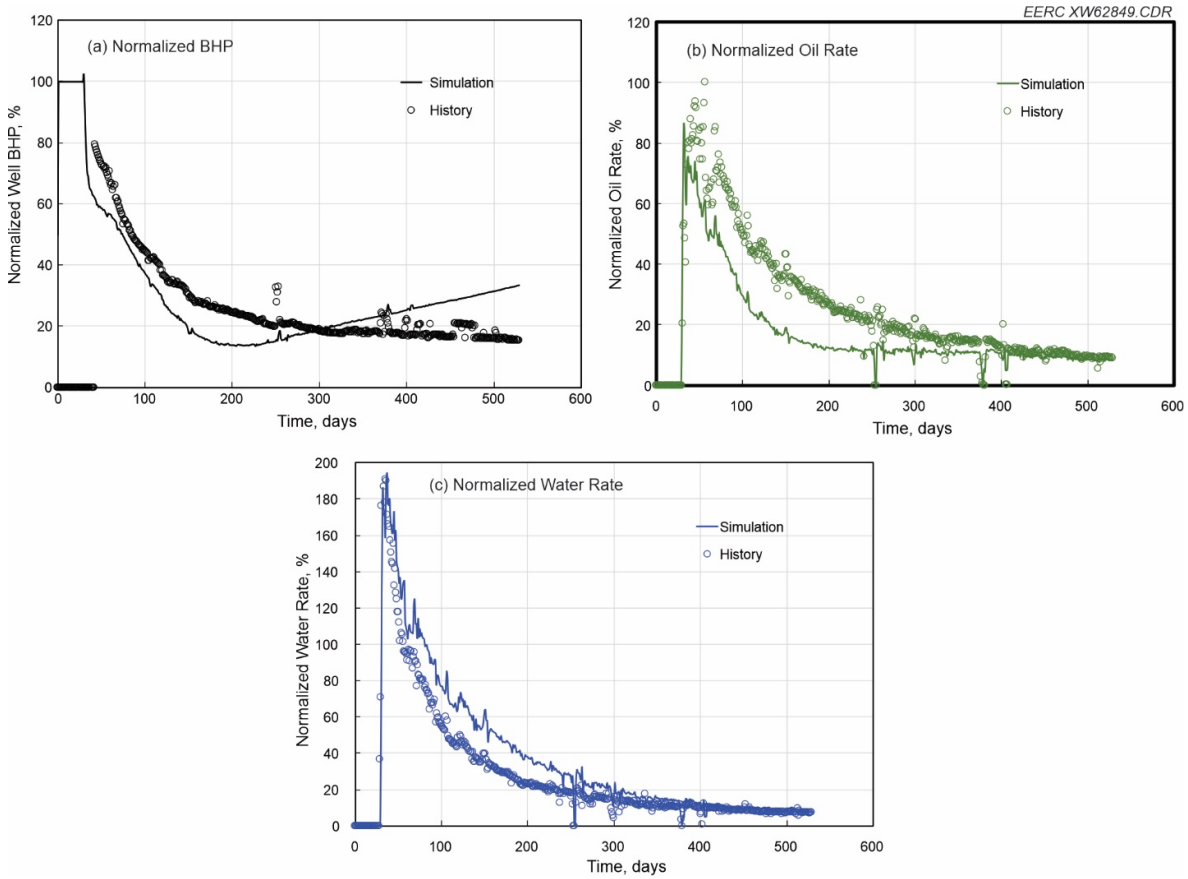


Figure 7. Manual HM results for Well 7SU showing the historical data (circles) and the simulation data (solid curves) for (**a**) normalized well BHP, (**b**) normalized oil rate, and (**c**) normalized water rate. Subplot (**a**) shows that the simulated well BHP deviated from the field data throughout production history. Subplots (**b**,**c**) show that the simulated oil and water rate deviated from the field historical data.

The purpose of manual HM was to generate a base case rather than to obtain a high-quality history match. The results of manual HM show that the BHP, oil rate, and water rate could be partially captured, but the simulated curves still had a deviation from

the historical data (Figure 7). The deviation may stem from uncertainties in matrix and hydraulic fracture properties.

Table 2. Basic reservoir and fracturing data in the reservoir simulation model.

Parameter	Unit	Value
Model length	ft	11,234
Model width	ft	1395
Model height	ft	802
Matrix permeability	mD	0.00046
Wellbore lateral length	ft	10,091
Number of stages	–	43
Number of hydraulic fractures	–	150
Average fracture spacing	ft	67
Fracture half-length	ft	400
Fracture height	ft	100
Fracture conductivity	mD-ft	200
Fracture aperture	ft	0.1

4. Automatic HM with EDFM–AI–AHM

HM is one of the most time-consuming tasks in the simulation process for unconventional reservoirs, especially when considerable uncertainties exist for fractures. Recently, an innovative method, EDFM–AI–AHM, was developed to assist the HM process by tuning fracture and matrix parameters automatically based on a set of parameters with ranges provided [36]. The method utilizes neural network (NN)-based proxy models by sampling stochastic reservoir model realizations and updating the proxy models using MCMC [37–43]. The approach has been applied to several field cases [10,43–45]. The performance of the EDFM–AI–AHM method is affected by the initial selection and ranges of the uncertainty parameters. Inappropriate selection or ranges of uncertainty parameters could lead to insufficient HM solutions [43]. In this study, multiple EDFM–AI–AHM scenarios with different selections and ranges of uncertainty parameters were designed to achieve an ensemble of HM solutions.

Figure 8 illustrates the general workflow employed in each EDFM–AI–AHM scenario [42]. The first step is to screen and identify uncertainty parameters that need to be included in the automatic history matching (AHM). One matrix parameter (matrix compaction coefficient) and seven hydraulic fracture parameters (fracture efficiency, fracture half-length, fracture height, fracture aperture or width, fracture conductivity, fracture water saturation, and fracture compaction coefficient) were identified as either fixed or uncertainty parameters and used to tune the EDFM–AI–AHM process.

These parameters were chosen because similar projects demonstrated that these parameters are often important for the HM process [39–43]. The ranges (minimum and maximum values) of the eight matrix and hydraulic fracturing parameters were established based on available HFTS-1-Midland field data, and these ranges are summarized in Table 3. The eight matrix and hydraulic fracturing parameters were assumed to follow a uniform prior distribution between the minimum and maximum values. The prior distribution assumed no central tendency, and then the MCMC process was used to converge toward a posterior distribution.

Initial cases that covered the input ranges of the uncertainty parameters were generated by Latin hypercube sampling (LHS) [46]. Fracture models were generated by EDFM and then integrated into simulation models for these initial cases, which were executed to generate simulation results. In the first iteration, the inputs and results of the initial simulation cases were extracted to train an initial set of neural networks (NNs). Next, the NN–MCMC algorithm [42] was run to perform HM automatically and select acceptable HM solutions. The obtained simulation inputs and results were then used to retrain the NN in the second iteration. The workflow would stop if no significant improvement was

detected in the latest iteration (stopping criteria); otherwise, the workflow would continue until the maximum number of iterations was reached.

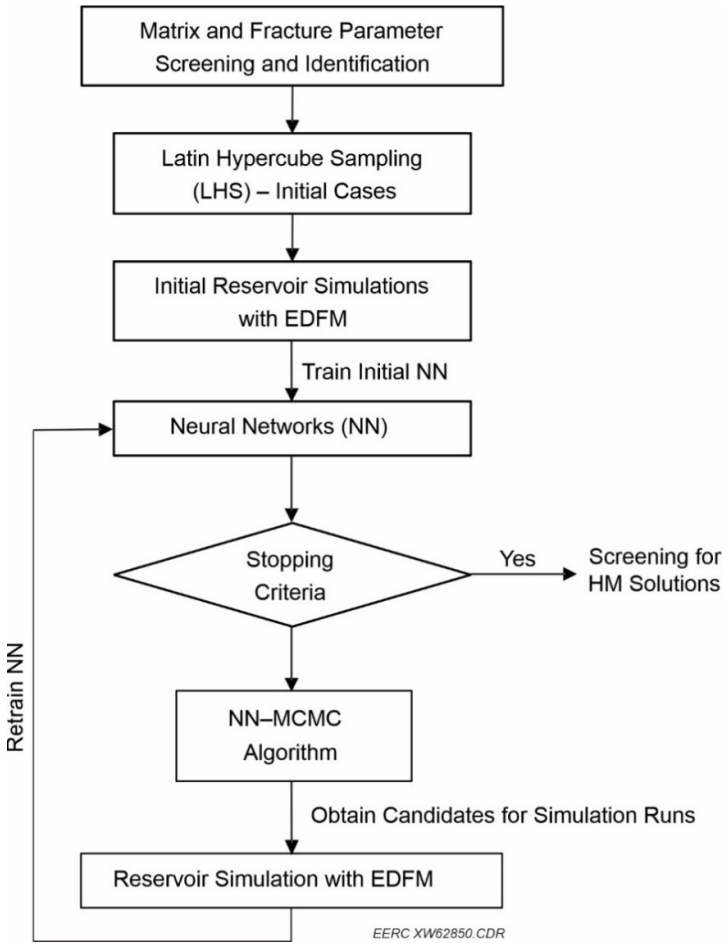


Figure 8. EDFM–AI–AHM workflow (modified from [42]).

Table 3. Ranges for the eight matrix and hydraulic fracturing parameters for EDFM–AI–AHM to generate HM solutions.

ML Variable Name	Parameter Name	Unit	Minimum	Maximum
X1	Fracture efficiency	Dimensionless	0.3	1
X2	Fracture half-length	ft	50	500
X3	Fracture height	ft	50	200
X4	Fracture aperture (or width)	ft	0.1	0.5
X5	Fracture conductivity	mD-ft	10	1300
X6	Fracture water saturation	frac	0.1	0.9
X7	Fracture compaction coefficient	Dimensionless	0.01	0.05
X8	Matrix compaction coefficient	Dimensionless	0.1	0.2

The quality of the HM was determined by the deviation between simulation results and historical (observed) data. The response variables (parameters) were historical oil rate, water rate, and well BHP, which were used to define the global objective function (GOF) as:

$$\mathrm{GOF} = \frac{\sum_{j=1}^{m}\sum_{i=1}^{n}\left[\frac{X_{ij,model}-X_{ij,history}}{X_{ij,history}}\times 100\right]^2 \times w_{ij}}{\sum_{j=1}^{m}\sum_{i=1}^{n} w_{ij}} \quad (3)$$

where i and j are the indices for data points and response parameters, respectively; m and n are the indices for the number of response parameters and data points, respectively; and $X_{ij,model}$, $X_{ij,history}$, and w_{ij} are the modeling data, historical data, and weight of data at index i of response parameter j, respectively.

The definition of the GOF in Equation (3) allows one global value to represent multiple local errors. During each iteration, the EDFM–AI–AHM workflow proposed a random number of samples, for example, 10,000 cases, to train and test NNs. The realizations with the lowest GOF values were retained and validated with reservoir simulations [42].

EDFM–AI–AHM Scenarios

Thirteen scenarios with different combinations of variable and fixed input parameters were designed, as shown in Table 4. X7 (fracture compaction coefficient) and X8 (matrix compaction coefficient) were included as variables in all the scenarios because they could characterize pressure-dependent matrix and fracture permeability changes. Providing a range of X7 and X8 promotes better bottomhole pressure HM performance. The other six fracture parameters were divided into three variables and three fixed parameters in each scenario with different arrangements so that the HM solutions would not be biased towards a single scenario of matrix and fracture property setups.

Table 4. Scenarios with different uncertainty parameter combinations to generate cases in EDFM–AI–AHM *.

Scenario	Uncertainty Parameters	Scenario	Uncertainty Parameters
1	X1, X2, X3, X7, X8	8	X1, X4, X5, X7, X8
2	X1, X2, X4, X7, X8	9	X1, X5, X6, X7, X8
3	X1, X2, X5, X7, X8	10	X2, X3, X4, X7, X8
4	X1, X2, X6, X7, X8	11	X2, X3, X5, X7, X8
5	X1, X3, X4, X7, X8	12	X2, X3, X6, X7, X8
6	X1, X3, X5, X7, X8	13	X2, X4, X6, X7, X8
7	X1, X3, X6, X7, X8		

* X1 (fracture efficiency), X2 (fracture half-length), X3 (fracture height), X4 (fracture aperture or width), X5 (fracture conductivity), X6 (fracture water saturation), X7 (fracture compaction coefficient), and X8 (matrix compaction coefficient).

In each scenario, 40 initial cases were generated via Latin hypercube sampling (LHS) and simulated via reservoir simulation with EDFM to train the initial neural network (NN). Twenty cases with the lowest GOFs were generated for each iteration step to be validated with reservoir simulations and retrain the NN. To reduce computational time, the maximum number of iterations was set to three; hence, a total of 100 cases were generated for each scenario (40 initial + [3 iterations $\times$ 20 cases]). Each scenario was run through the full set of cases, so the total number of cases generated from the 13 scenarios was 1300 simulations.

Although the EDFM–AI–AHM workflow could potentially improve HM quality by retaining realizations with the lowest GOFs during each iteration, some retained cases could still possibly have high GOF values, and it would be less flexible to apply a single GOF threshold to treat simulations in all the scenarios. Therefore, the individual objective function (IOF) that measured the error for each response parameter was calculated after the iterations were completed in each scenario to further screen the optimum HM solutions, as shown in Equation (4).

$$\mathrm{IOF}_j = \frac{\sum_{i=1}^{n} \left[\frac{X_{ij,model} - X_{ij,history}}{X_{ij,history}} \times 100 \right]^2 \times w_{ij}}{\sum_{i=1}^{n} w_{ij}} \quad (4)$$

where IOF_j is the individual objective function for the response parameter j [47].

The IOF threshold for each response parameter was decided by comparing the EDFM–AI–AHM-generated 100 simulation results with the historical data for each scenario. A higher IOF value allows more cases to be further retained. In this study, the IOF threshold

for well BHP was set to be from 60% to 80%, while that for oil and water rates was set to be from 30% to 50%. The higher threshold value was assigned to well BHP because the match of well BHP was not easy to achieve due to the assumption that pressure interference was not considered in the model.

Among the 1300 simulation results, 358 simulation cases that met the IOF criteria for the response parameters of the 13 scenarios were retained and used to generate posterior distributions of the matrix and fracture properties and to obtain a "best fit" reservoir simulation model used for the production forecasts. After the iterations were completed in each scenario, the data for model setup, including the range of uncertainty inputs, proxy locations, and number of cases in each iteration, were collected and saved. The prior and posterior distribution data were generated along with descriptive statistics including the 10th percentile (P10), the 50th percentile (P50) (or median), and the 90th percentile (P90) values that were determined from the posterior distributions. The solution curves set containing the historical data and the simulation solutions were also collected and saved.

5. HM Improvement Using EDFM–AI–AHM

5.1. Initial Simulation Cases

Parameter values generated via Latin hypercube sampling (LHS) were used to create 40 initial simulation cases for Well 7SU BHP, oil rate, and water rate (Figure 9). The field and simulation data in Figure 9 were normalized using the same method as that applied for Figure 7. In each panel, the curves show the simulation results and the hollow circles show the historical production data (history). As shown in the figures, the simulation results covered the full range of production history.

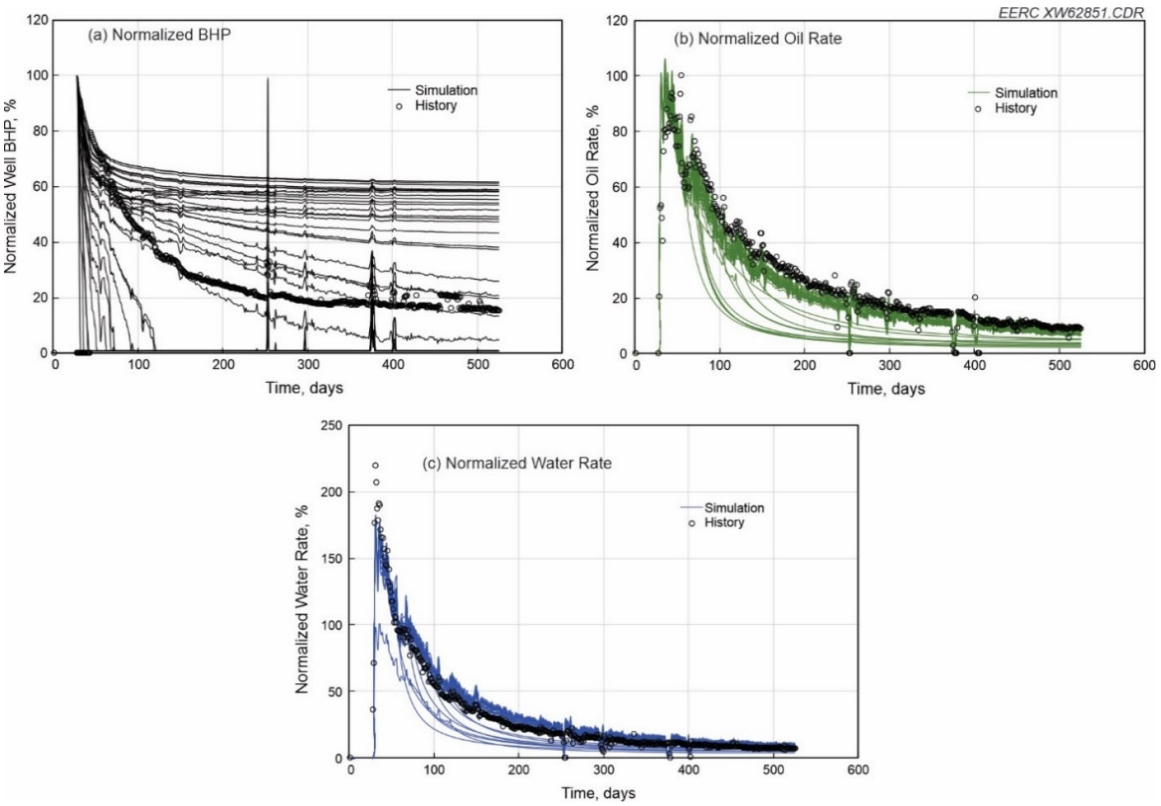


Figure 9. Initial simulation results and historical data for Well 7SU for (**a**) normalized BHP, (**b**) normalized oil rate, and (**c**) normalized water rate. (**a**) shows that three simulated BHP curves were close to field data. (**b**,**c**) show that 31 simulated oil and water rate curves were reasonably matched with the field data.

Table 5 shows the parameters and their ranges to set up Scenario 1 in EDFM–AI–AHM. For Scenario 1, the uncertainty parameters used to tune the automatic history matching

(AHM) process were fracture efficiency (X1), fracture half-length (X2), fracture height (X3), fracture compaction coefficient (X7), and matrix compaction coefficient (X8). The other three parameters—fracture aperture (X4), fracture conductivity (X5), and fracture water saturation (X6)—were set as fixed parameters with values of 0.1 ft, 150 mD-ft, and 0.5, respectively. The input parameter ranges for Scenarios 2–13 can be found in Tables A1–A12 in Appendix A.

Table 5. EDFM–AI–AHM parameters and ranges (minimum/maximum or fixed value) for Scenario 1.

ML Variable Name	Parameter Name	Type	Unit	Minimum	Maximum	Value
X1	Fracture efficiency	Uncertain	Dimensionless	0.3	1	–
X2	Fracture half-length	Uncertain	ft	50	500	–
X3	Fracture height	Uncertain	ft	50	200	–
X7	Fracture compaction coefficient	Uncertain	Dimensionless	0.01	0.05	–
X8	Matrix compaction coefficient	Uncertain	Dimensionless	0.1	0.2	–
X4	Fracture aperture	Fixed	ft	–	–	0.1
X5	Fracture conductivity	Fixed	mD-ft	–	–	150
X6	Fracture water saturation	Fixed	frac	–	–	0.5

Parameter values generated via LHS were used to create 40 initial simulation cases for Well 7SU BHP, oil rate, and water rate (Figure 9). The field and simulation data in Figure 9 were normalized using the same method as that applied for Figure 7. In each panel, the curves show the simulation results and the hollow circles show the historical production data (history). As shown in the figures, the simulation results covered the full range of production history. While 31 cases had similar oil and water production trends compared to the historical data, only three cases presented a slight deviation from the BHP; thus, up to three cases can be retained in the initial iteration.

The gas rate was not used as a matching parameter since only a single well was considered in the model, while gas may flow across multiple wells in the actual field because of the higher mobility of gas compared to that of oil and water. The inputs and results of these 40 initial simulation cases for all the match points were used to train the initial neural network (NN). Then, the NN–MCMC algorithm was used to perform the automatic history matching (AHM).

5.2. NN–MCMC and AHM

For Scenario 1, 22 solutions that met the IOF criteria for response parameters were screened by the NN–MCMC algorithms during the iterations (Figure 10). The field and simulation data of BHP, oil rate, and water rate in Figure 10 were normalized with the same approach as that applied to Figures 7 and 9. The IOF thresholds for oil rate, water rate, and well BHP are 30%, 30%, and 60%, respectively. Compared with the manual HM results shown in Figure 7 and the initial simulation results shown in Figure 9, the HM quality significantly improved after implementing the EDFM–AI–AHM workflow. The simulation results of BHP, oil rate, and water rate matched well with the historical data, as illustrated in Figure 10a–c, respectively. Compared to manual HM, the results were significantly improved by utilizing the EDFM–AI–AHM method.

5.3. Fracture Parameter Property Distributions

Figure 11 shows the prior and posterior property distribution of fracture half-length, fracture height, hydraulic fracturing (HF) efficiency, matrix compaction coefficient, and fracture compaction coefficient for the 22 solutions of Scenario 1 that had an acceptable GOF criterion. The results show that the posterior distribution (orange bars in the figure) of all five uncertainty parameters was different from the prior distribution (gray bars in the figure, which denote a uniform distribution between the minimum and maximum values).

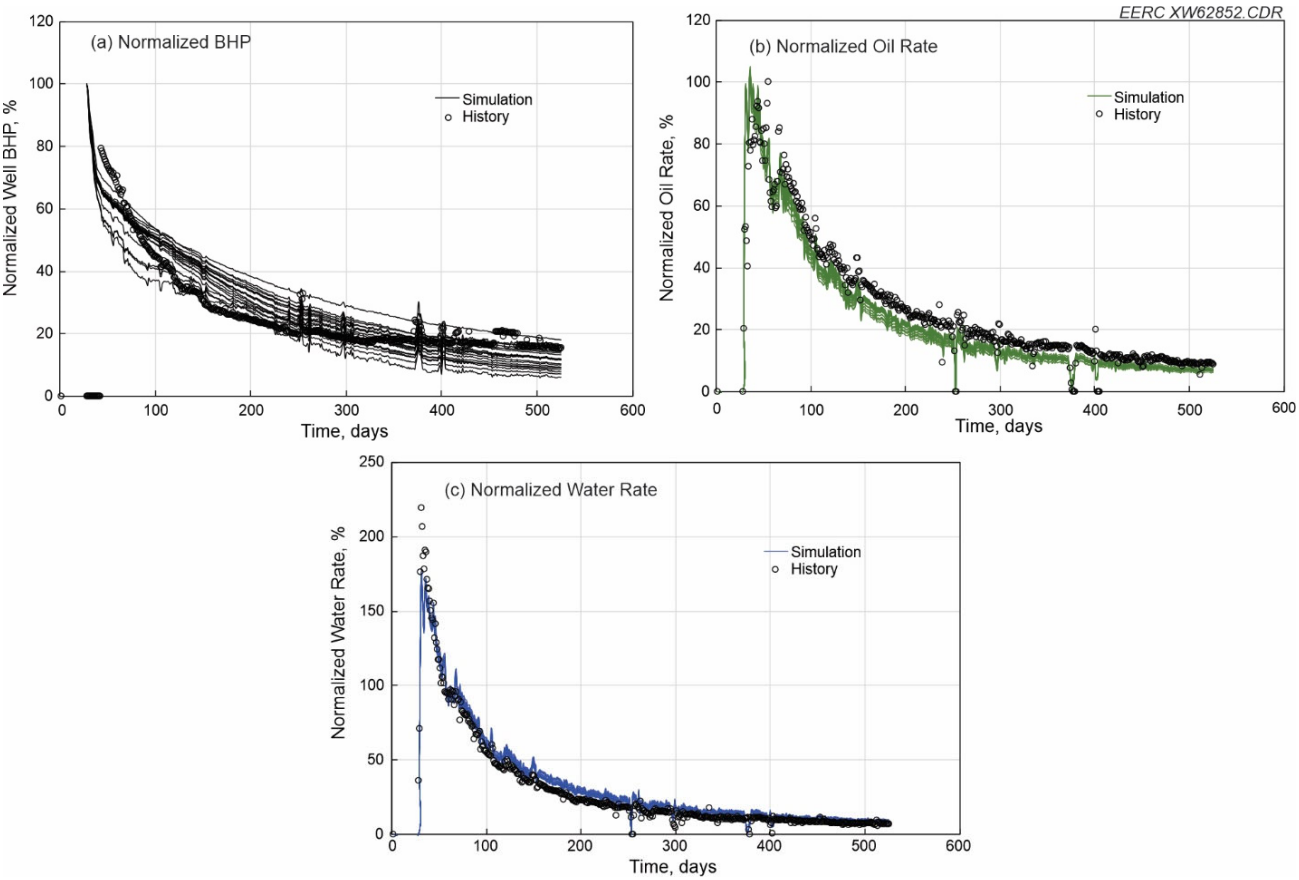


Figure 10. Results from the 22 HM solutions screened by EDFM–AI–AHM for Well 7SU under Scenario 1: (**a**) normalized BHP, (**b**) normalized oil rate, and (**c**) normalized water rate. (**a**–**c**) show that the simulated BHP, oil rate, and water rate curves matched well with the field data.

Higher histogram probability was observed for the posterior distribution in a smaller range of uncertainty parameters compared to the prior distribution. The results indicate that the initial range of uncertainty parameters could be optimized to improve HM quality. For example, Figure 11a shows the 40 initial simulation cases had a uniform distribution of fracture height in the range of 50–200 ft, whereas the posterior distribution of fracture height had posterior P10 to P90 values of 90 and 129 ft, respectively, and a median of 110 ft. The results indicate that modifying the range of fracture height from 50–200 ft to 90–129 ft could potentially improve HM quality. Similarly, the posterior P10 and P90 values in Figure 11b imply that modifying the range of fracture half-length from 50–500 ft to 127–327 ft could potentially improve HM quality. Figure 11b also shows that the posterior distribution is not compact within the range between P10 and P90, and the posterior probability is 0 for fracture half-length in the range of approximately 208–298 ft. Running more iterations to generate more solutions may be an approach to further eliminate the 0-probability range between P10 and P90.

The best case for Scenario 1 was observed from the combination of fracture half-length, fracture height, HF efficiency, matrix compaction coefficient, and fracture compaction coefficient of 189.36 ft, 109.67 ft, 0.481, 0.11, and 0.038 respectively, as illustrated by the red vertical line in Figure 11. The prior and posterior distributions of the input parameters for Scenarios 2–13 can be found in Figures A1–A12 in Appendix A.

Table 6 summarizes the number of retained HM solutions for all 13 scenarios, which shows that a total of 358 HM solutions were retained from the studied scenarios and 1300 reservoir simulation cases. These 358 reservoir simulations from EDFM–AI–AHM were a set of input/output (I/O) matrices from physics-based (i.e., reservoir simulations) solutions to well production performance, given values of the matrix and fracture network

properties. These physics-based I/O matrices provide insights into the uncertainty in the matrix and fracture network properties, which can inform the subsequent production forecast and EOR strategy optimization. In addition, the I/O matrices can be further used as training and testing data for other ML workflows outside of EDFM–AI–AHM.

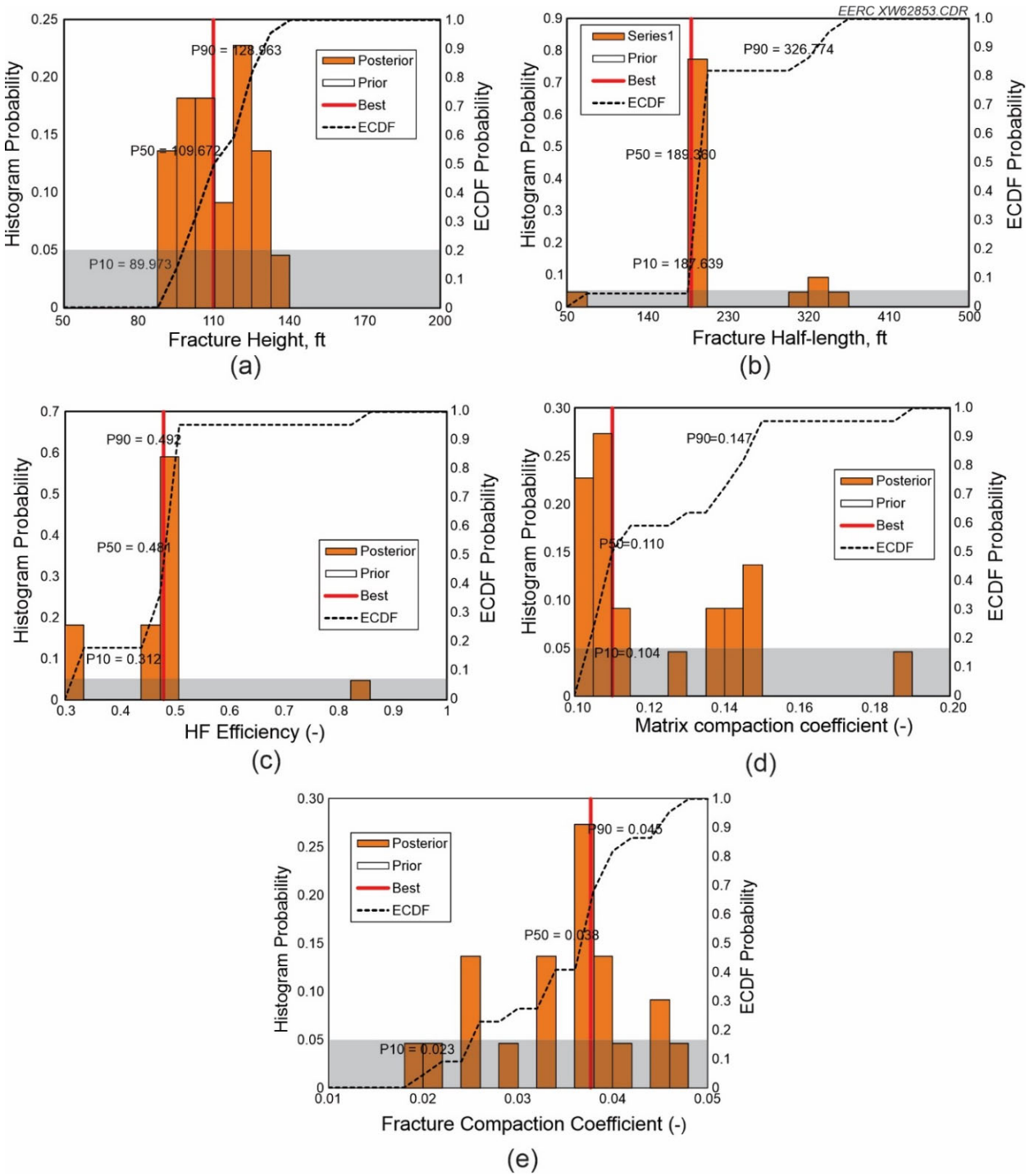


Figure 11. Prior (gray bars) and posterior (orange bars) distribution of uncertainty parameters for the 22 solutions of Scenario 1: (**a**) fracture half-length, (**b**) fracture height, (**c**) HF efficiency, (**d**) matrix compaction coefficient, and (**e**) fracture compaction coefficient. ECDF = empirical cumulative distribution function.

Table 6. Number of HM solutions for models with different variable combinations.

Scenario	Variable Combination	Number of Retained HM Solutions
1	X1, X2, X3, X7, X8	22
2	X1, X2, X4, X7, X8	20
3	X1, X2, X5, X7, X8	30
4	X1, X2, X6, X7, X8	6
5	X1, X3, X4, X7, X8	43
6	X1, X3, X5, X7, X8	37
7	X1, X3, X6, X7, X8	42
8	X1, X4, X5, X7, X8	59
9	X1, X5, X6, X7, X8	15
10	X2, X3, X4, X7, X8	4
11	X2, X3, X5, X7, X8	31
12	X2, X3, X6, X7, X8	8
13	X2, X4, X6, X7, X8	41
	Total	358

6. Production Forecast and EOR Strategy Optimization

The results of cumulative oil production for the 358 retained solutions were compared with the historical data to evaluate the HM performance after the EDFM–AI–AHM workflow, as shown in Figure 12a. While the EDFM–AI–AHM workflow significantly improved HM results compared to the manual HM and initial simulation cases for the production forecast and EOR optimization, the solutions were further screened to improve the accuracy of simulated oil production using the following two criteria:

(1) The error E_h of cumulative oil production between the simulated solutions and the historical data at the end of production history is less than 10%.
(2) The root mean square error (RMSE) between the simulated solutions and the historical data for cumulative oil production is less than 10 Mstb (thousand stock tank barrels).

The E_h and $RMSE$ values are calculated using the following equations.

$$E_h = \frac{|Q_{se} - Q_{he}|}{Q_{he}} \times 100\% \tag{5}$$

$$RMSE = \sqrt{\frac{\sum_{i=1}^{n}[Q_s(i) - Q_h(i)]^2}{n}} \tag{6}$$

where Q_{se} and Q_{he} are cumulative oil production at the end of production history for simulation and historical data, respectively; $Q_s(i)$ and $Q_h(i)$ are cumulative oil production at data point i for simulation and historical results, respectively; and n is the total number of cumulative production data points.

The calculated E_h and RMSE values for manual HM are 34% and 38%, respectively. The results show that the manual HM does not meet the E_h and RMSE criteria. As shown in Figure 12a, most retained HM solutions show better HM performance than that of the manual HM.

Of the 358 retained EDFM–AI–AHM solutions, 57 were selected using the additional criteria of E_h and RMSE. The results of the 57 selected solutions after further screening are shown in Figure 12b. These 57 selected solutions can be used in future works to further investigate the effects of different fracture and matrix properties on production prediction and enhanced oil recovery (EOR) performance. The best match representing the solution that has the minimum RMSE (red line in Figure 12b) was used for production forecast and EOR optimization in this study.

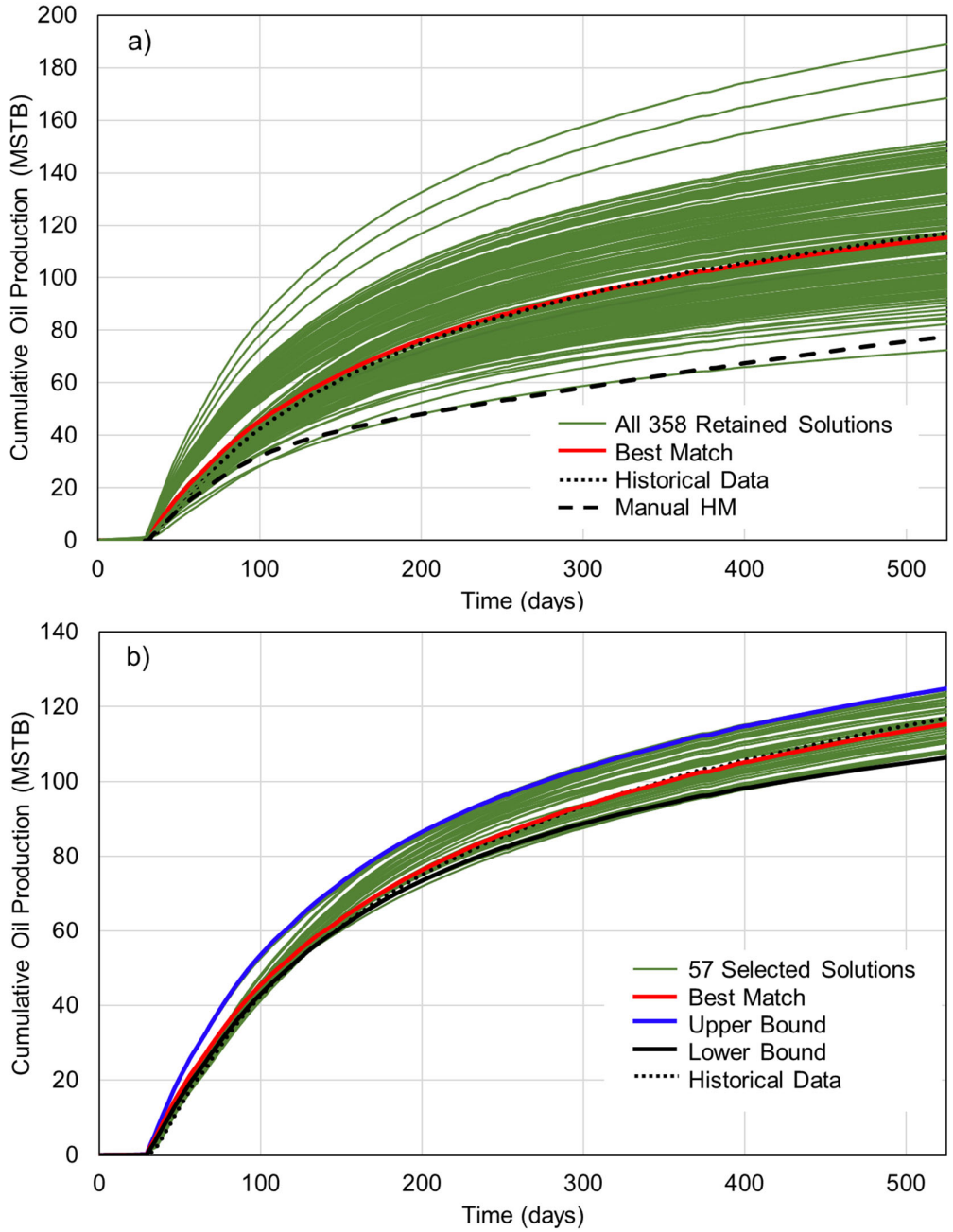


Figure 12. Cumulative oil production for historical data and (**a**) all 358 retained solutions from the EDFM–AI–AHM workflow and (**b**) 57 selected solutions using the additional criteria of E_{lt} and RMSE showing the upper and lower bounds and best match.

6.1. Production Prediction via Primary Recovery

Based on the best-match HM case, a predictive case for pressure depletion (with minimum BHP fixed at 300 psi for 10 years) was simulated to observe the oil production and drainage behavior of the well. The pressure distribution around Well 7SU at different time steps is shown in Figure 13, which indicates that most of the pressure depletion happened around the region with hydraulic fractures in the first several years of production. The difference between 5 and 10 years of prediction is small (Figure 13b,c) compared to the difference between the end of production history and the first 5 years of prediction (Figure 13a,b), as the drainage area (yellow and green area close to the blue lines with A pressure decline greater than 500 psi) is difficult to extend into the matrix because of the low permeability of the Upper Wolfcamp geological zone.

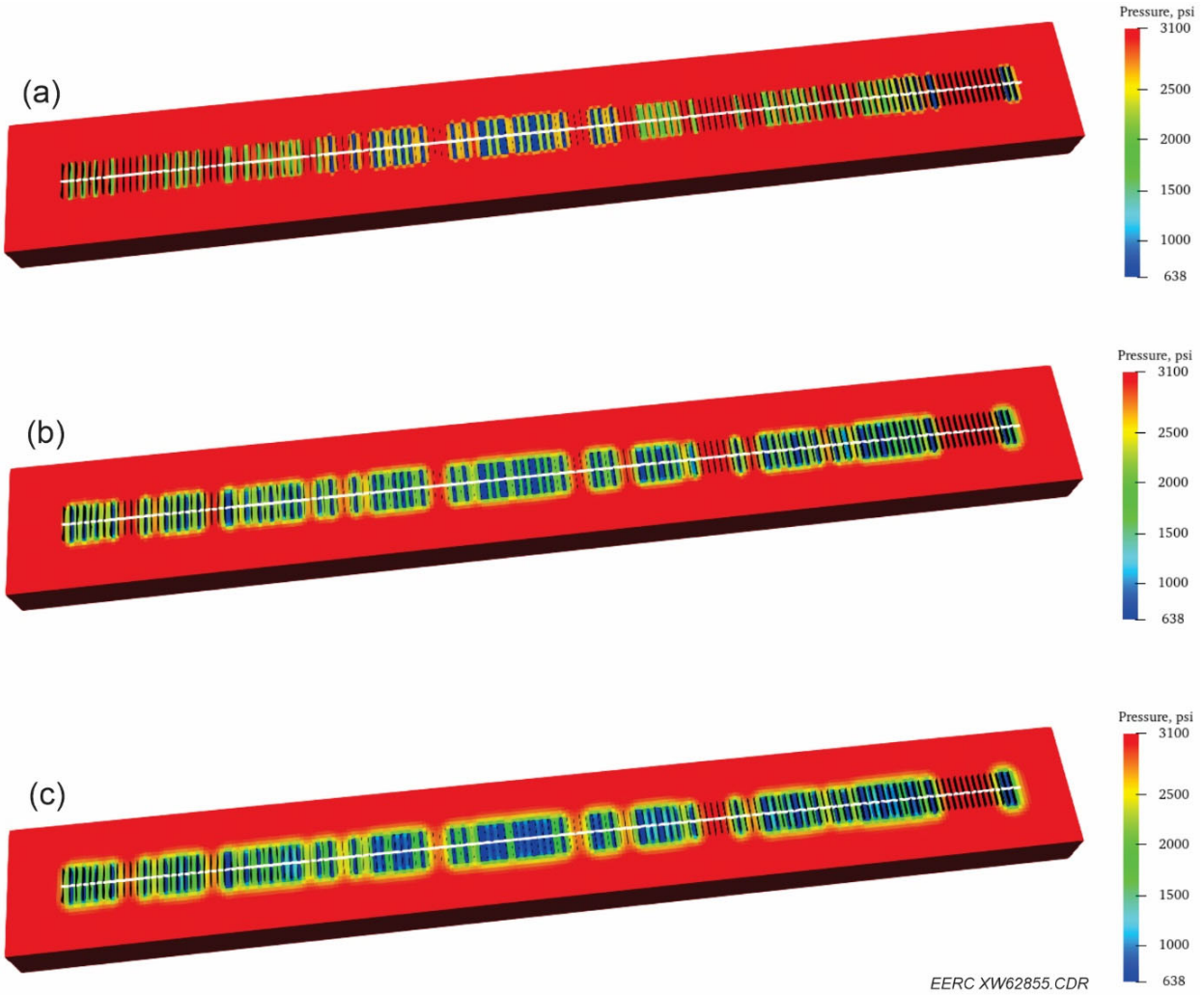


Figure 13. Pressure distribution around Well 7SU for Scenario 1 at different time steps: (**a**) end of production history (1.5 years), (**b**) 5 years of prediction, and (**c**) 10 years of prediction. The drainage area (yellow and green area close to the blue lines) expanded from the end of production to 5 years of prediction. The change in drainage area was not significant from 5 to 10 years of prediction. Well toe is on the right side of each subfigure.

6.2. EOR via CO_2 Huff 'n Puff (HnP)

Since the drainage area is difficult to extend into the reservoir matrix for primary production because of the depletion of pressure in the near-wellbore region, CO_2 HnP was explored as an EOR method to improve oil production. Five predictive cases were designed based on the best HM case to investigate the effects of gas injection rate on EOR performance. The injection rate varied from 2 to 25 million standard cubic feet per day (MMscfd), with injection, soaking, and production times of 30, 0, and 30 days, respectively, and a total cycle time of 60 days (Table 7). EOR performance was compared against the baseline case of primary production with no EOR. Two years of CO_2 HnP were simulated for each of the five cases. Figure 14 shows that an increased gas injection rate contributes to more incremental oil production. This is because a high gas injection rate is beneficial to providing pressure support in the hydraulic fractures and the drainage area near fractures so that the injected gas can penetrate the low-permeability reservoir matrix to interact with oil for EOR. While the 2, 4, and 8 MMscfd cases were not significantly different from the baseline case with no EOR (gray, blue, and green lines in Figure 14), the 18 and 25 MMscfd cases showed significantly greater cumulative oil production over the 2-year period (orange and red lines in Figure 14). For example, the cumulative oil production over the 2-year

period for the baseline case with no EOR (pressure depletion) was 144 Mstb, while the cumulative oil production over the 2-year period for the 18 and 25 MMscfd cases was 153 and 164 Mstb, respectively, for increases of 6.4% and 14% over the baseline case.

Table 7. Input parameters for different HnP cases.

Parameter	Value
EOR Operational Time	2 years
Injection Rate	2, 4, 8, 18, 25 MMscfd
Injection Time	30 days/cycle
Soaking Time	0 days/cycle
Production Time	30 days/cycle
Injection Gas	CO_2
Maximum Gas Injection Pressure Constraint	7500 psi
Minimum Production Pressure Constraint	300 psi

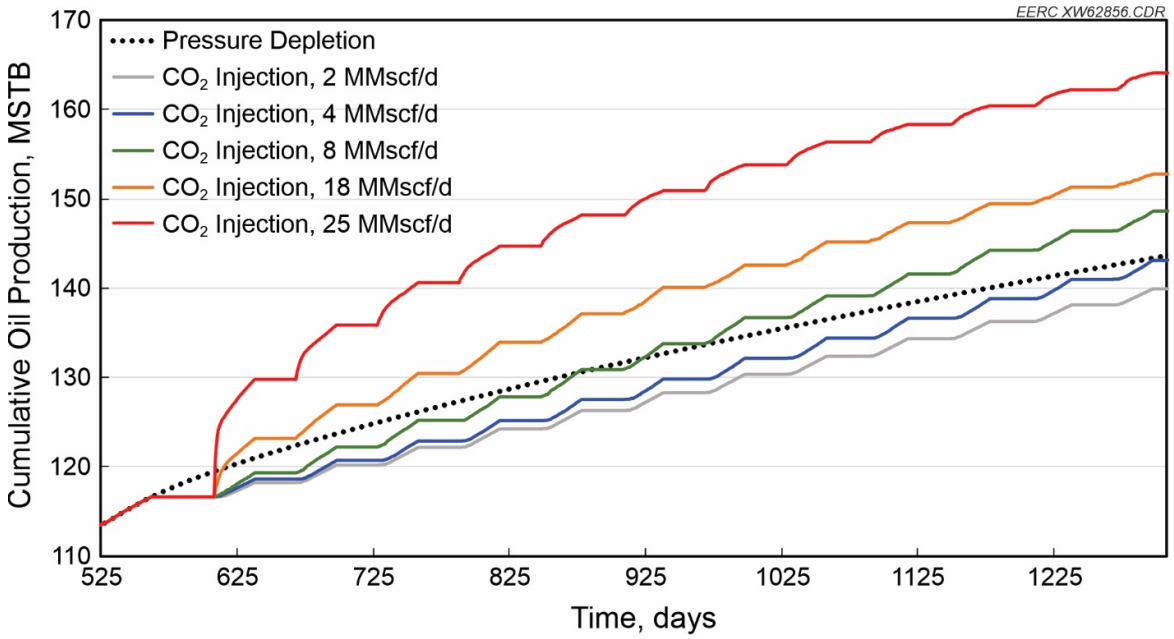


Figure 14. Effect of gas injection rate on EOR performance of Well 7SU. The pressure depletion case represents the 2-year primary production prediction case.

In conventional high-permeability reservoirs, CO_2 injection is commonly performed at the pressure of slightly above minimum miscibility pressure (MMP), since increasing pressure above MMP does not improve oil recovery [48–50]. In contrast, for CO_2 injection in unconventional reservoirs, the oil recovery is a strong function of injection pressure, and increasing injection pressure, regardless of MMP, contributes to higher oil recovery [50–56]. This is because the pressure above MMP allows gas to enter the nanoscale pores to "unlock" and extract the residual oil. Figure 15 shows that a higher CO_2 injection rate contributes to higher injection pressure in each cycle.

Table 8 summarizes the simulation results of maximum injection pressure during the HnP process, total oil production after the end of simulation, and incremental oil recovery for the five HnP cases. Case 0 corresponds to the pressure depletion scenario as the base case. The incremental oil recovery is negative for Cases 1 and 2 because the oil increase during the production period cannot compensate for the loss of production during the injection period.

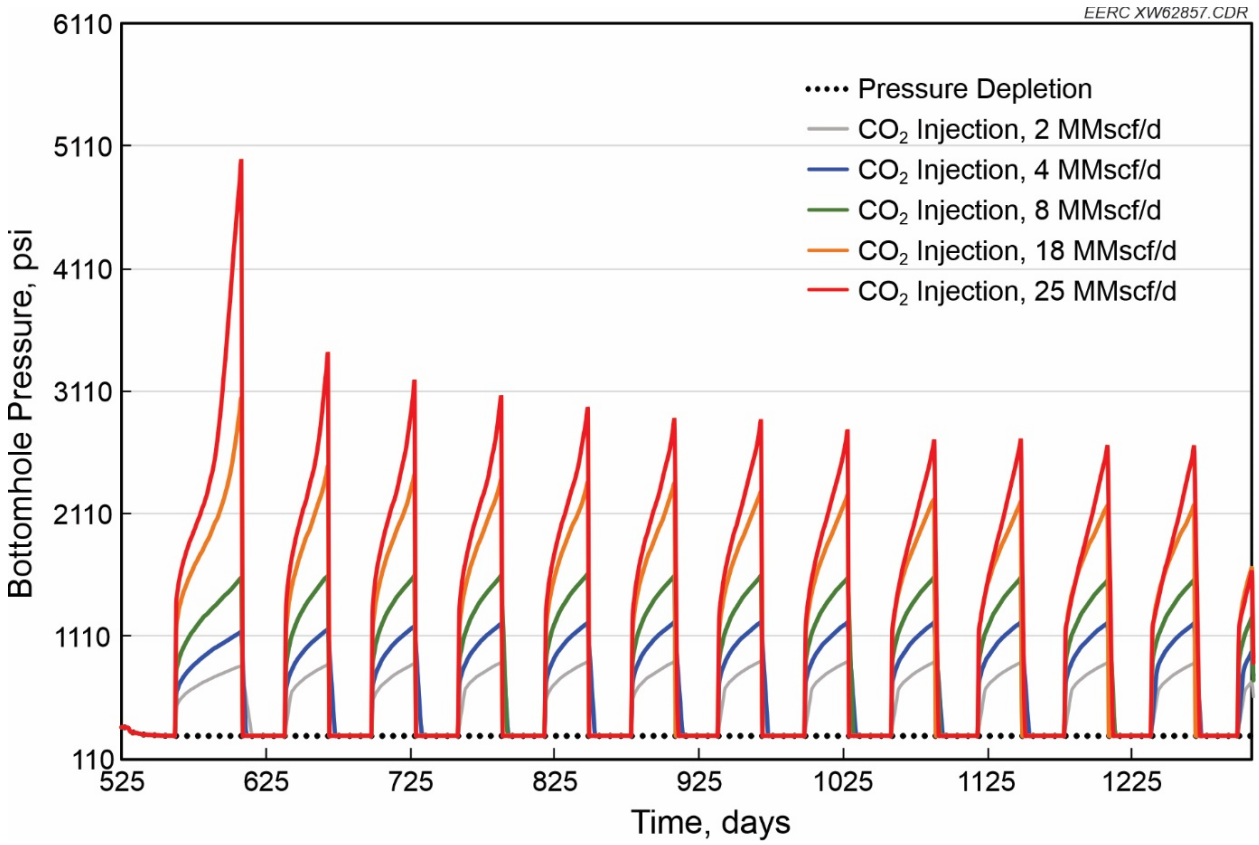


Figure 15. Effect of gas injection rate on the well BHP for Well 7SU.

Table 8. Simulation results for different CO_2 HnP cases.

Case No.	Injection Rate, MMscfd	Maximum Injection Pressure, psi	Total Oil Production, Mstb	Incremental Oil Recovery, % *
0	–	–	144	–
1	2	909	140	−2.6
2	4	1227	143	−0.4
3	8	1620	149	3.5
4	18	3052	153	6.4
5	25	4989	164	14

* Incremental oil recovery is calculated by comparing the total oil production of each case with that of Case 0.

The MMP for CO_2 and Wolfcamp oil tested by different researchers ranges from 1620 to 3706 psi [57–59]. Figure 16 shows that the simulated maximum injection pressure covers the range of MMP from the cited references [57–59]. The simulation results shown in Table 8 and Figure 16 further confirm that it does not matter if the maximum injection is above or below MMP; a higher maximum injection pressure contributes to more oil production. Another conclusion that can be drawn from the simulation results is that a gas injection rate of greater than 4 MMscfd is required to achieve meaningful incremental oil production, as suggested in Table 8.

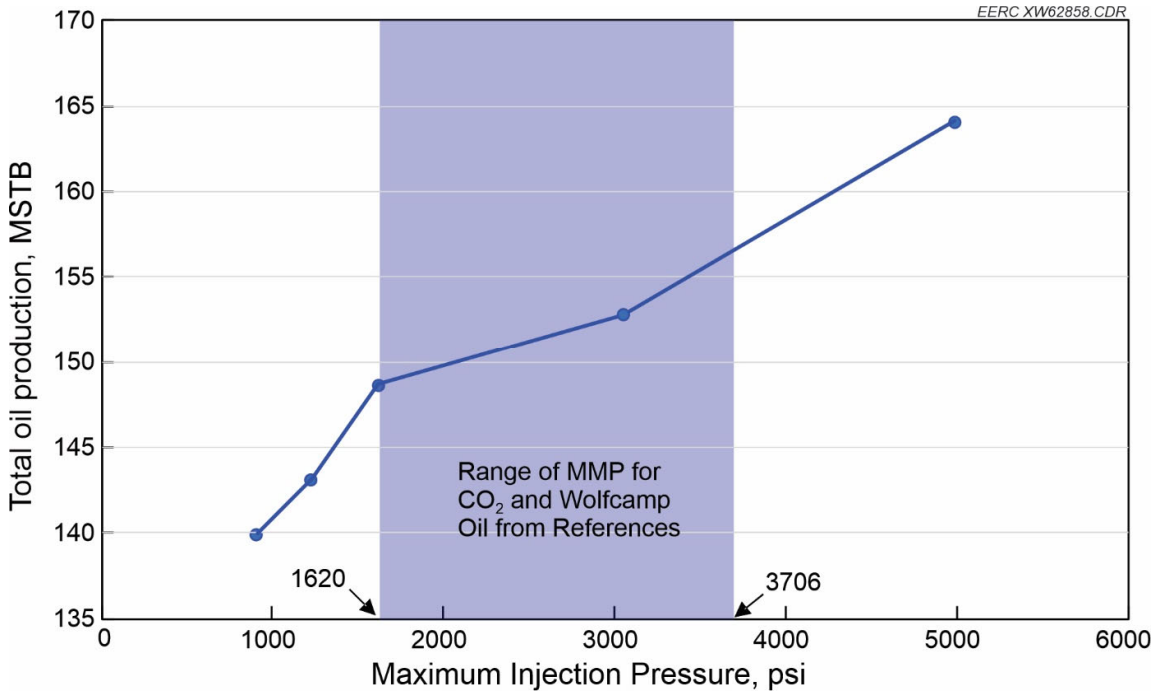


Figure 16. Effect of maximum CO_2 injection pressure during the whole HnP process on total oil production after 2 years of HnP.

7. Conclusions

A reservoir simulation model was developed based on the geological properties of the Wolfcamp Formation from the geologic model and fracture properties generated by an EDFM method. The reservoir simulation model was processed by the EDFM–AI–AHM approach to generate a set of reservoir simulations that explores the parameter space of the fracture network properties and generates physics-based solutions to well production given the fracture network properties.

A total of 358 HM solutions were obtained from 1300 reservoir simulations generated by 13 EDFM–AI–AHM scenarios. These solutions ensure better characterization of the matrix and fracture uncertainties. The matrix and property information and the corresponding simulated production results can be used as the input and output parameters for the development of other machine learning (ML) algorithms. The retained 358 HM solutions were further screened using the cumulative oil production error (E_h) and root mean square error (RMSE) criteria to obtain 57 solutions. The selected 57 solutions are suitable candidates for production prediction and EOR optimization.

The solution with the best HM performance was used for further simulations of production forecast and CO_2 EOR strategy optimization. The results of the production forecast via primary recovery indicate that the drainage area is difficult to extend into the low-permeability reservoir matrix to generate sustainable oil production. The simulation results of CO_2 EOR showed that a higher gas injection rate contributes to more oil production regardless of MMP. A gas injection rate of greater than 4 MMscfd is required for the well to improve oil production. A gas injection rate of 25 MMscfd could improve oil production by 14% compared to the pressure depletion (no EOR) scenario.

Author Contributions: Funding acquisition, S.K.B.; Investigation, X.W.; Methodology, X.W. and X.Y.; Resources, L.J.; Supervision, L.J. and N.A.A.; Visualization, X.W.; Writing—original draft, X.W.; Writing—review & editing, L.J., N.A.A., S.K.B., X.Y. and J.Z. All authors have read and agreed to the published version of the manuscript.

Funding: This work was funded by DOE NETL, an agency of the United States Government, through a support contract with Leidos Research Support Team (LRST). This work was performed in support

of the U.S. Department of Energy (DOE) Office of Fossil Energy's Carbon Storage Research Program through the National Energy Technology Laboratory (NETL) in ongoing research under prime contract no. 89243318CFE000003. Neither the United States Government nor any agency thereof, nor any of their employees, nor LRST, nor any of their employees, makes any warranty, expressed or implied, or assumes any legal liability or responsibility for the accuracy, completeness, or usefulness of any information, apparatus, product, or process disclosed, or represents that its use would not infringe privately owned rights. Reference herein to any specific commercial product, process, or service by trade name, trademark, manufacturer, or otherwise, does not necessarily constitute or imply its endorsement, recommendation, or favoring by the United States Government or any agency thereof. The views and opinions of authors expressed herein do not necessarily state or reflect those of the United States Government or any agency thereof.

Acknowledgments: This work was completed as part of the Science-informed Machine learning to Accelerate Real Time decision making for Carbon Storage (SMART-CS) Initiative (https://edx.netl.doe.gov/smart/, accessed on 11 October 2022). The content is solely the responsibility of the authors and does not necessarily represent the official views of DOE NETL. This work was also supported by the State Energy Research Center of North Dakota. The modeling work conducted under this program was made possible by the contributions of software licenses from Computer Modelling Group Ltd., SimTech, and Schlumberger.

Conflicts of Interest: The authors declare no conflict of interest.

Appendix A

Table A1. Ranges of input variables for Scenario 2 to run AHM workflow.

ML Variable	Parameter Name	Type	Unit	Minimum	Maximum	Value
X1	Fracture efficiency	Uncertain	Dimensionless	0.3	1	–
X2	Fracture half-length	Uncertain	ft	50	500	–
X4	Fracture aperture	Uncertain	ft	0.1	0.5	–
X7	Fracture compaction coefficient	Uncertain	Dimensionless	0.01	0.05	–
X8	Matrix compaction coefficient	Uncertain	Dimensionless	0.1	0.2	–
X3	Fracture height	Fixed	ft	–	–	106
X5	Fracture conductivity	Fixed	mD-ft	–	–	200
X6	Fracture water saturation	Fixed	frac	–	–	0.4

Table A2. Ranges of input variables for Scenario 3 to run AHM workflow.

ML Variable	Parameter Name	Type	Unit	Minimum	Maximum	Value
X1	Fracture efficiency	Uncertain	Dimensionless	0.3	1	–
X2	Fracture half-length	Uncertain	ft	50	500	–
X5	Fracture conductivity	Uncertain	mD-ft	10	300	–
X7	Fracture compaction coefficient	Uncertain	Dimensionless	0.01	0.05	–
X8	Matrix compaction coefficient	Uncertain	Dimensionless	0.1	0.2	–
X3	Fracture height	Fixed	ft	–	–	106
X4	Fracture aperture	Fixed	ft	–	–	0.1
X6	Fracture water saturation	Fixed	frac	–	–	0.5

Table A3. Ranges of input variables for Scenario 4 to run AHM workflow.

ML Variable	Parameter Name	Type	Unit	Minimum	Maximum	Value
X1	Fracture efficiency	Uncertain	Dimensionless	0.3	1	–
X2	Fracture half-length	Uncertain	ft	50	500	–
X6	Fracture water saturation	Uncertain	frac	0.1	0.9	–
X7	Fracture compaction coefficient	Uncertain	Dimensionless	0.01	0.05	–

Table A3. *Cont.*

ML Variable	Parameter Name	Type	Unit	Minimum	Maximum	Value
X8	Matrix compaction coefficient	Uncertain	Dimensionless	0.1	0.2	–
X3	Fracture height	Fixed	ft	–	–	106
X4	Fracture aperture	Fixed	ft	–	–	0.1
X5	Fracture conductivity	Fixed	mD-ft	–	–	200

Table A4. Ranges of input variables for Scenario 5 to run AHM workflow.

ML Variable	Parameter Name	Type	Unit	Minimum	Maximum	Value
X1	Fracture efficiency	Uncertain	Dimensionless	0.3	1	–
X3	Fracture height	Fixed	ft	50	200	–
X4	Fracture aperture	Fixed	ft	0.1	0.5	–
X7	Fracture compaction coefficient	Uncertain	Dimensionless	0.01	0.05	–
X8	Matrix compaction coefficient	Uncertain	Dimensionless	0.1	0.2	–
X2	Fracture half-length	Uncertain	ft	–	–	220
X5	Fracture conductivity	Uncertain	mD-ft	–	–	110
X6	Fracture water saturation	Fixed	frac	–	–	0.3

Table A5. Ranges of input variables for Scenario 6 to run AHM workflow.

ML Variable	Parameter Name	Type	Unit	Minimum	Maximum	Value
X1	Fracture efficiency	Uncertain	Dimensionless	0.3	1	–
X3	Fracture height	Uncertain	ft	50	200	–
X5	Fracture conductivity	Uncertain	mD-ft	150	700	–
X7	Fracture compaction coefficient	Uncertain	Dimensionless	0.01	0.05	–
X8	Matrix compaction coefficient	Uncertain	Dimensionless	0.1	0.2	–
X2	Fracture half-length	Fixed	ft	–	–	250
X4	Fracture aperture	Fixed	ft	–	–	0.1
X6	Fracture water saturation	Fixed	frac	–	–	0.6

Table A6. Ranges of input variables for Scenario 7 to run AHM workflow.

ML Variable	Parameter Name	Type	Unit	Minimum	Maximum	Value
X1	Fracture efficiency	Uncertain	Dimensionless	0.3	1	–
X3	Fracture height	Uncertain	ft	50	200	–
X6	Fracture water saturation	Uncertain	frac	0.1	0.9	–
X7	Fracture compaction coefficient	Uncertain	Dimensionless	0.01	0.05	–
X8	Matrix compaction coefficient	Uncertain	Dimensionless	0.1	0.2	–
X2	Fracture half-length	Fixed	ft	–	–	150
X4	Fracture aperture	Fixed	ft	–	–	0.1
X5	Fracture conductivity	Fixed	mD-ft	–	–	175

Table A7. Ranges of input variables for Scenario 8 to run AHM workflow.

ML Variable	Parameter Name	Type	Unit	Minimum	Maximum	Value
X1	Fracture efficiency	Uncertain	Dimensionless	0.3	1	–
X4	Fracture aperture	Uncertain	ft	0.1	0.5	–
X5	Fracture conductivity	Uncertain	mD-ft	100	500	–
X7	Fracture compaction coefficient	Uncertain	Dimensionless	0.01	0.05	–
X8	Matrix compaction coefficient	Uncertain	Dimensionless	0.1	0.2	–
X2	Fracture half-length	Fixed	ft	–	–	85
X3	Fracture height	Fixed	ft	–	–	150
X6	Fracture water saturation	Fixed	frac	–	–	0.3

Table A8. Ranges of input variables for Scenario 9 to run AHM workflow.

ML Variable	Parameter Name	Type	Unit	Minimum	Maximum	Value
X1	Fracture efficiency	Fixed	Dimensionless	0.3	1	–
X5	Fracture conductivity	Fixed	mD-ft	10	150	–
X6	Fracture water saturation	Uncertain	frac	0.5	0.9	–
X7	Fracture compaction coefficient	Uncertain	Dimensionless	0.01	0.05	–
X8	Matrix compaction coefficient	Uncertain	Dimensionless	0.1	0.2	–
X2	Fracture half-length	Uncertain	ft	–	–	189
X3	Fracture height	Fixed	ft	–	–	106
X4	Fracture aperture	Uncertain	ft	–	–	0.1

Table A9. Ranges of input variables for Scenario 10 to run AHM workflow.

ML Variable	Parameter Name	Type	Unit	Minimum	Maximum	Value
X2	Fracture half-length	Uncertain	ft	50	200	–
X3	Fracture height	Uncertain	ft	50	200	–
X4	Fracture aperture	Uncertain	ft	0.1	0.5	–
X7	Fracture compaction coefficient	Uncertain	Dimensionless	0.01	0.05	–
X8	Matrix compaction coefficient	Uncertain	Dimensionless	0.1	0.2	–
X1	Fracture efficiency	Fixed	Dimensionless	–	–	1
X5	Fracture conductivity	Fixed	mD-ft	–	–	126.5
X6	Fracture water saturation	Fixed	frac	–	–	0.324

Table A10. Ranges of input variables for Scenario 11 to run AHM workflow.

ML Variable	Parameter Name	Type	Unit	Minimum	Maximum	Value
X2	Fracture half-length	Uncertain	ft	50	500	–
X3	Fracture height	Uncertain	ft	50	200	–
X5	Fracture conductivity	Uncertain	mD-ft	200	1000	–
X7	Fracture compaction coefficient	Uncertain	Dimensionless	0.01	0.05	–
X8	Matrix compaction coefficient	Uncertain	Dimensionless	0.1	0.2	–
X1	Fracture efficiency	Fixed	Dimensionless	–	–	0.5
X4	Fracture aperture	Fixed	ft	–	–	0.3
X6	Fracture water saturation	Fixed	frac	–	–	0.7

Table A11. Ranges of input variables for Scenario 12 to run AHM workflow.

ML Variable	Parameter Name	Type	Unit	Minimum	Maximum	Value
X2	Fracture half-length	Uncertain	ft	50	500	–
X3	Fracture height	Uncertain	ft	50	200	–
X6	Fracture water saturation	Uncertain	frac	0.5	0.9	–
X7	Fracture compaction coefficient	Uncertain	Dimensionless	0.01	0.05	–
X8	Matrix compaction coefficient	Uncertain	Dimensionless	0.1	0.2	–
X1	Fracture efficiency	Fixed	Dimensionless	–	–	0.6
X4	Fracture aperture	Fixed	ft	–	–	0.2
X5	Fracture conductivity	Fixed	mD-ft	–	–	150

Table A12. Ranges of input variables for Scenario 13 to run AHM workflow.

ML Variable	Parameter Name	Type	Unit	Minimum	Maximum	Value
X2	Fracture half-length	Uncertain	ft	50	500	–
X4	Fracture aperture	Uncertain	ft	0.1	0.5	–
X6	Fracture water saturation	Uncertain	frac	0.5	0.9	–

Table A12. *Cont.*

ML Variable	Parameter Name	Type	Unit	Minimum	Maximum	Value
X7	Fracture compaction coefficient	Uncertain	Dimensionless	0.01	0.05	–
X8	Matrix compaction coefficient	Uncertain	Dimensionless	0.1	0.2	–
X1	Fracture efficiency	Fixed	Dimensionless	–	–	0.5
X3	Fracture height	Fixed	ft	–	–	130
X5	Fracture conductivity	Fixed	mD-ft	–	–	170

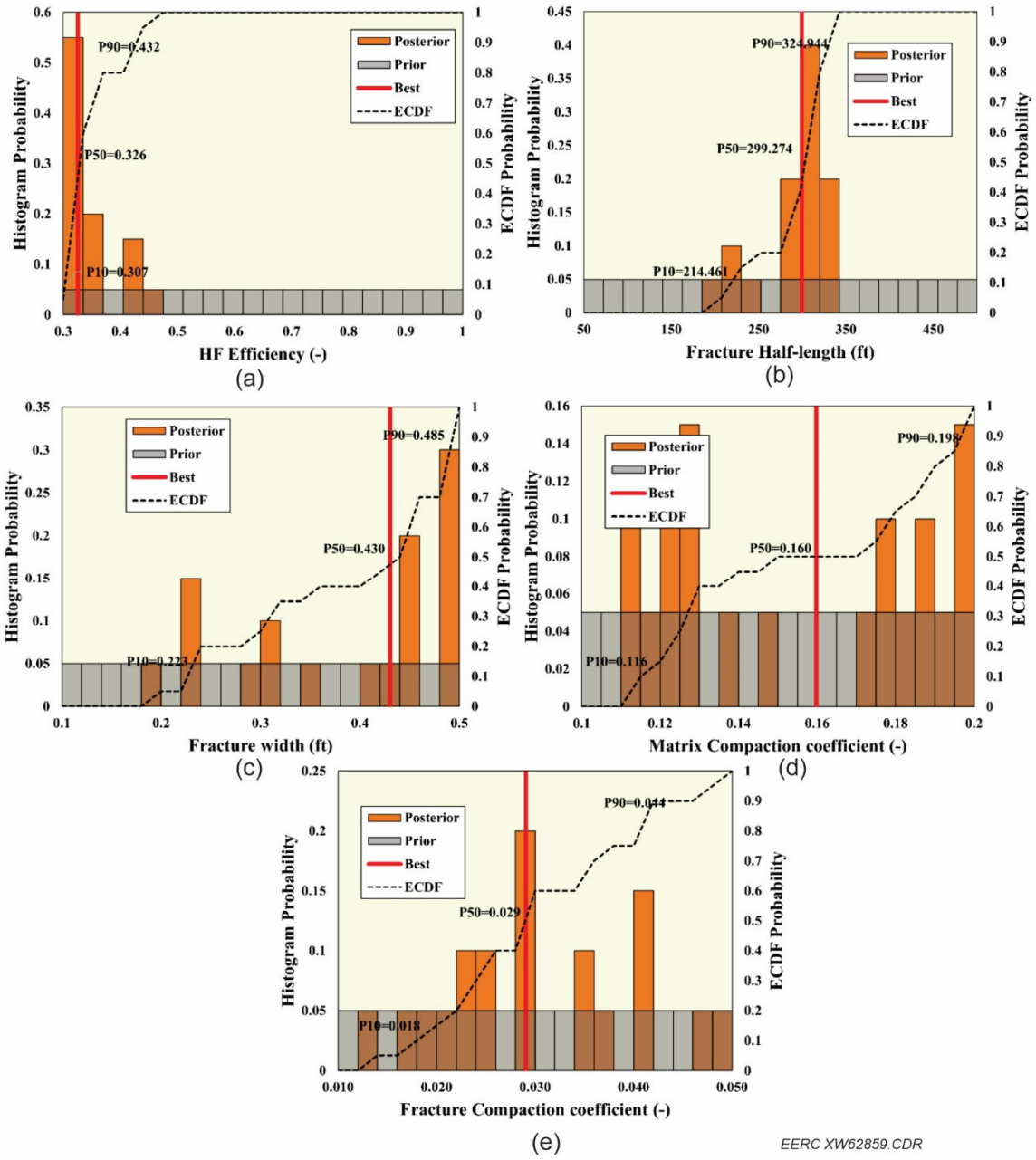


Figure A1. Prior and posterior distribution of uncertainty parameters for the 20 solutions of Scenario 2: (**a**) HF efficiency, (**b**) fracture half−length, (**c**) fracture width, (**d**) matrix compaction coefficient, and (**e**) fracture compaction coefficient.

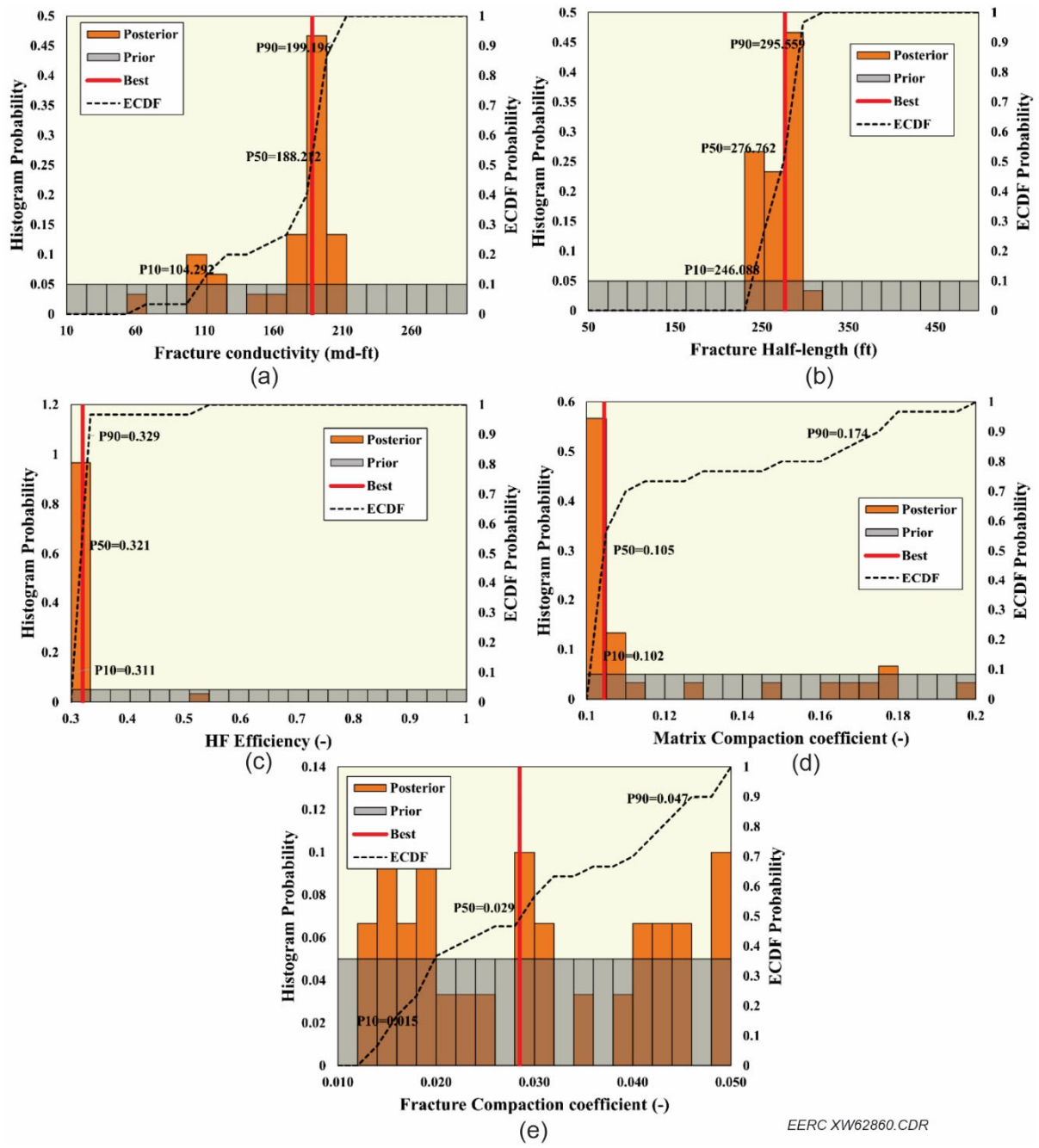


Figure A2. Prior and posterior distribution of uncertainty parameters for the 30 solutions of Scenario 3: (**a**) fracture conductivity, (**b**) fracture half−length, (**c**) HF efficiency, (**d**) matrix compaction coefficient, and (**e**) fracture compaction coefficient.

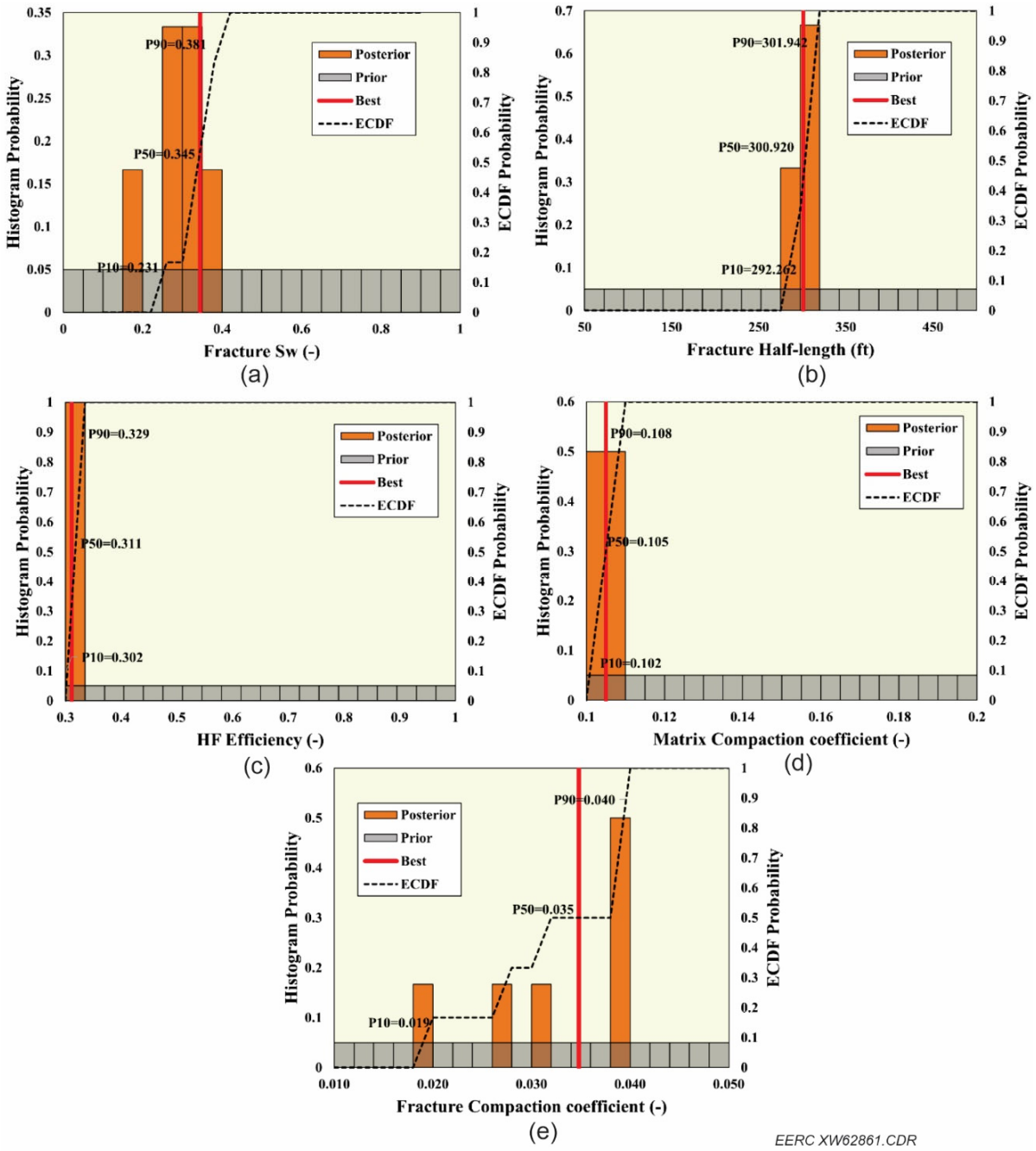


Figure A3. Prior and posterior distribution of uncertainty parameters for the six solutions of Scenario 4: (**a**) fracture initial water saturation, (**b**) fracture half−length, (**c**) HF efficiency, (**d**) matrix compaction coefficient, and (**e**) fracture compaction coefficient.

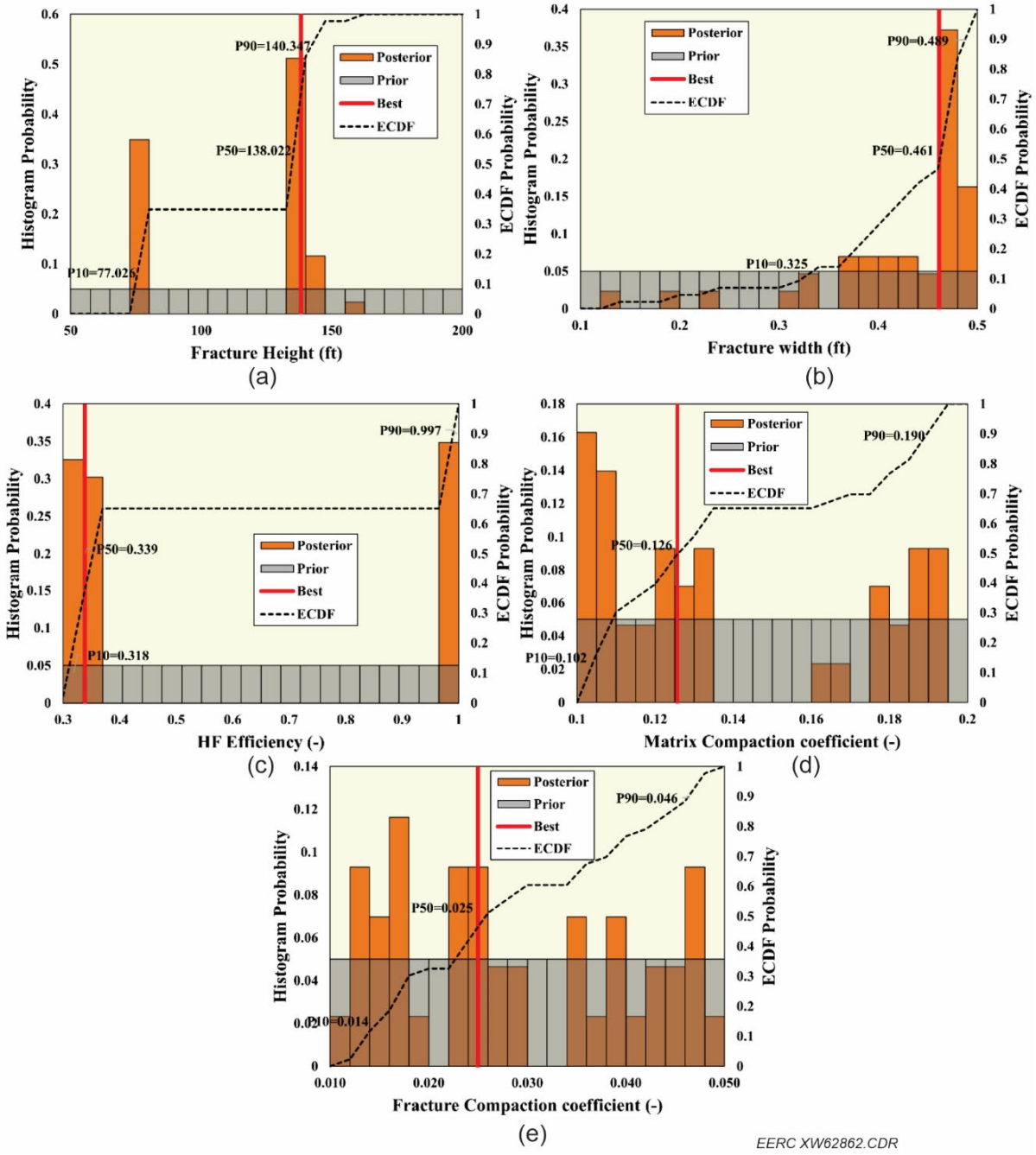


Figure A4. Prior and posterior distribution of uncertainty parameters for the 43 solutions of Scenario 5: (**a**) fracture height, (**b**) fracture width, (**c**) HF efficiency, (**d**) matrix compaction coefficient, and (**e**) fracture compaction coefficient.

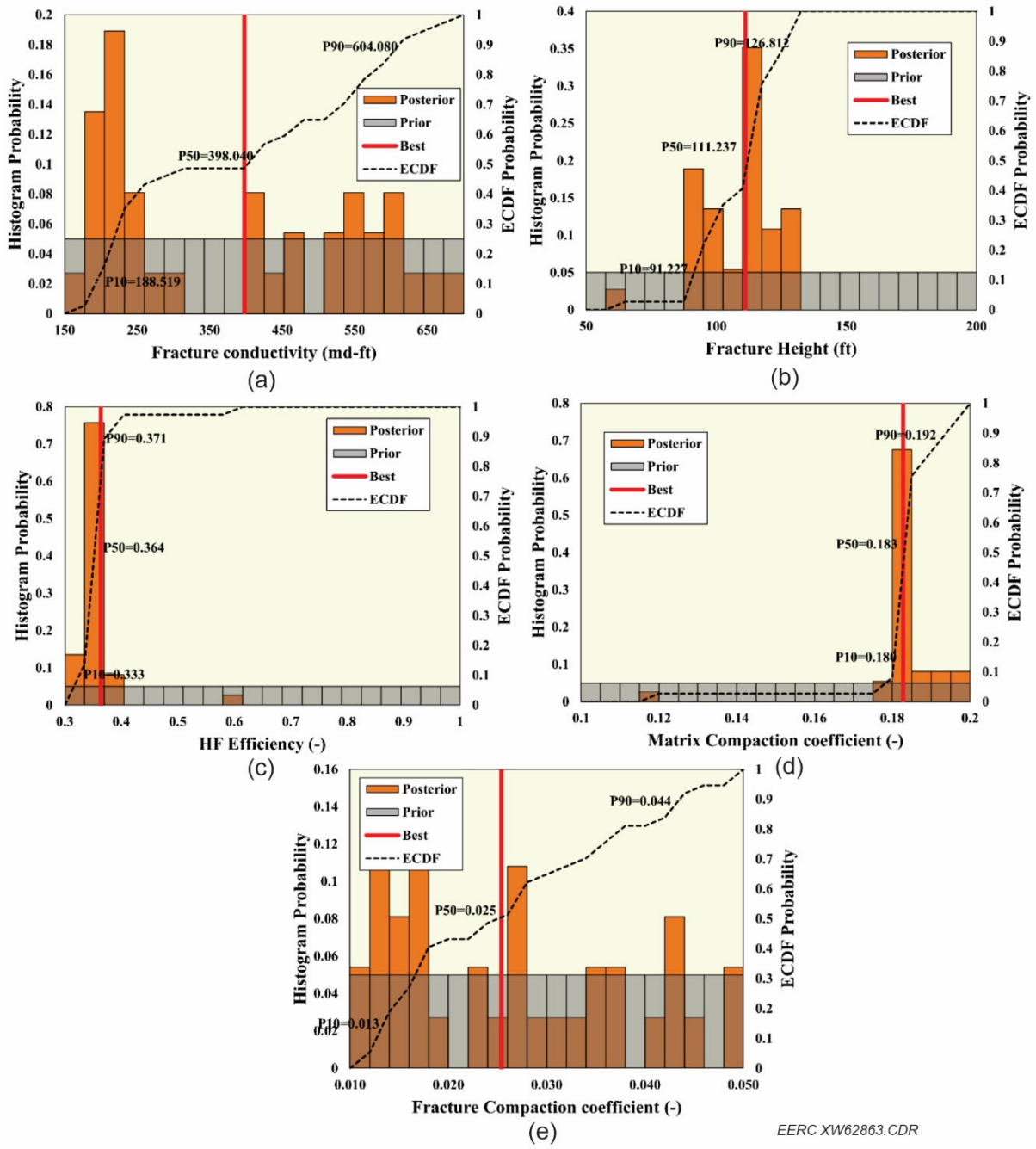


Figure A5. Prior and posterior distribution of uncertainty parameters for the 37 solutions of Scenario 6: (**a**) fracture conductivity, (**b**) fracture height, (**c**) HF efficiency, (**d**) matrix compaction coefficient, and (**e**) fracture compaction coefficient.

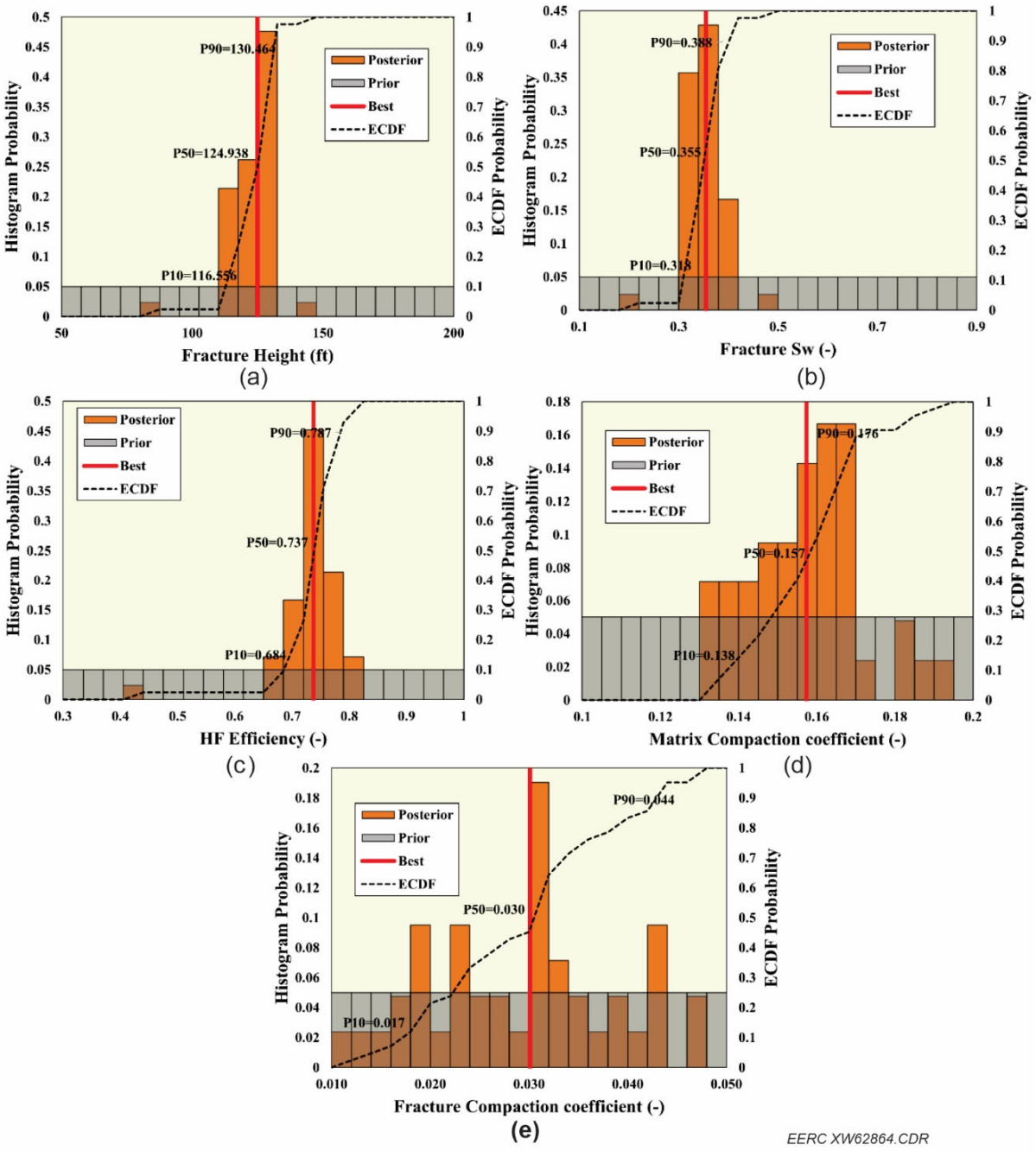


Figure A6. Prior and posterior distribution of uncertainty parameters for the 42 solutions of Scenario 7: (**a**) fracture height, (**b**) fracture initial water saturation, (**c**) HF efficiency, (**d**) matrix compaction coefficient, and (**e**) fracture compaction coefficient.

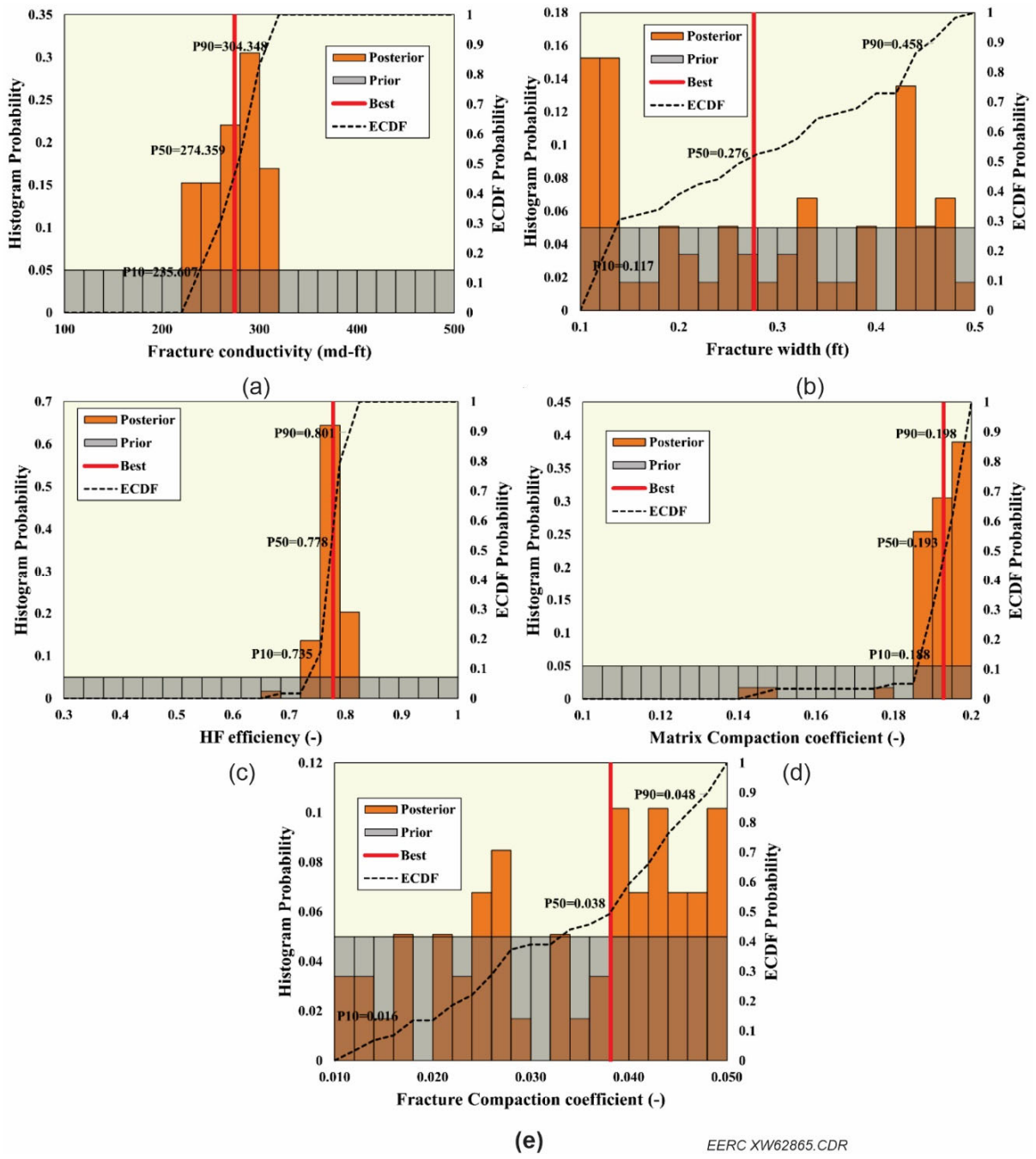


Figure A7. Prior and posterior distribution of uncertainty parameters for the 59 solutions of Scenario 8: (**a**) fracture conductivity, (**b**) fracture width, (**c**) HF efficiency, (**d**) matrix compaction coefficient, and (**e**) fracture compaction coefficient.

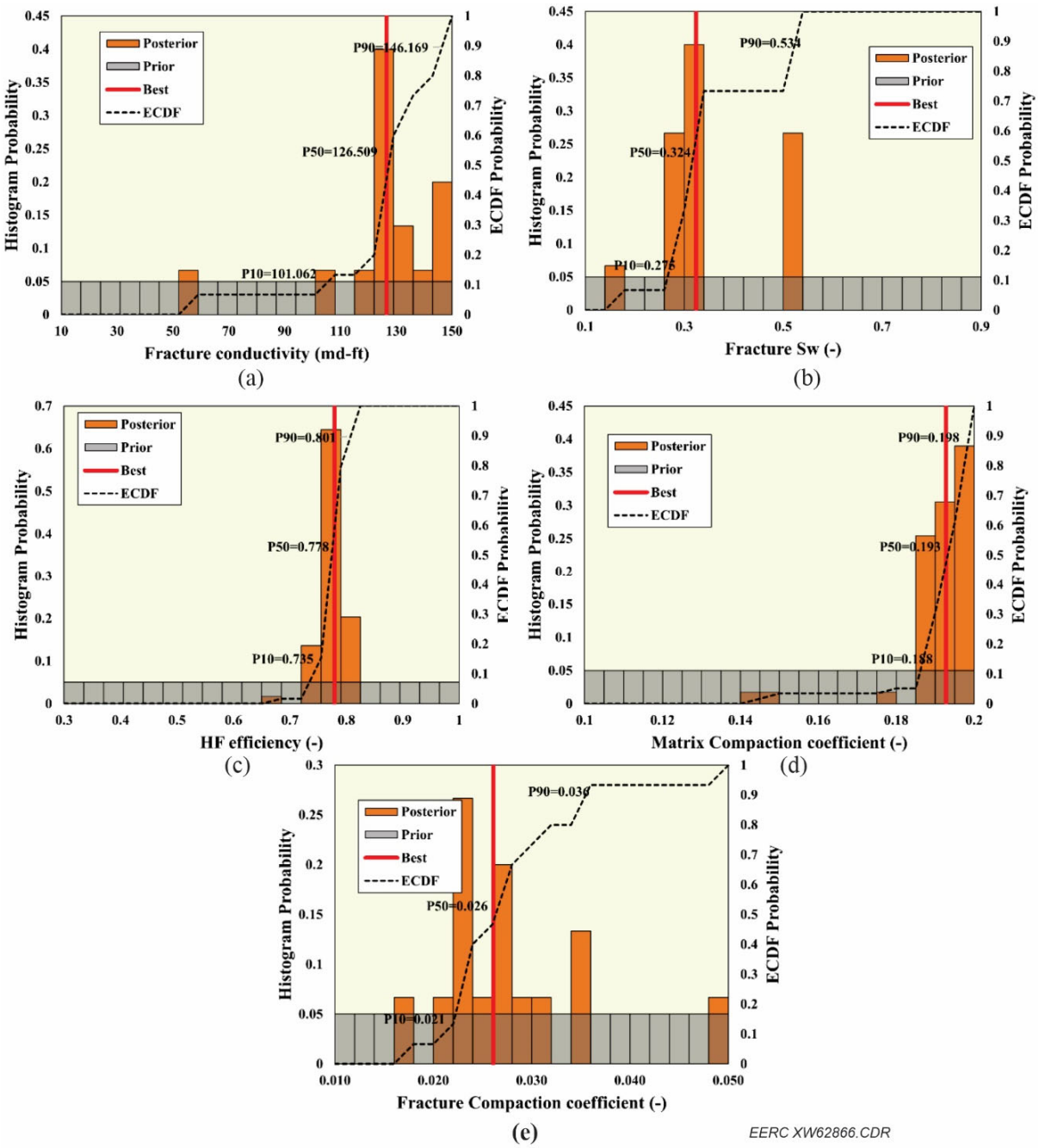


Figure A8. Prior and posterior distribution of uncertainty parameters for the 15 solutions of Scenario 9: (**a**) fracture conductivity, (**b**) fracture initial water saturation, (**c**) HF efficiency, (**d**) matrix compaction coefficient, and (**e**) fracture compaction coefficient.

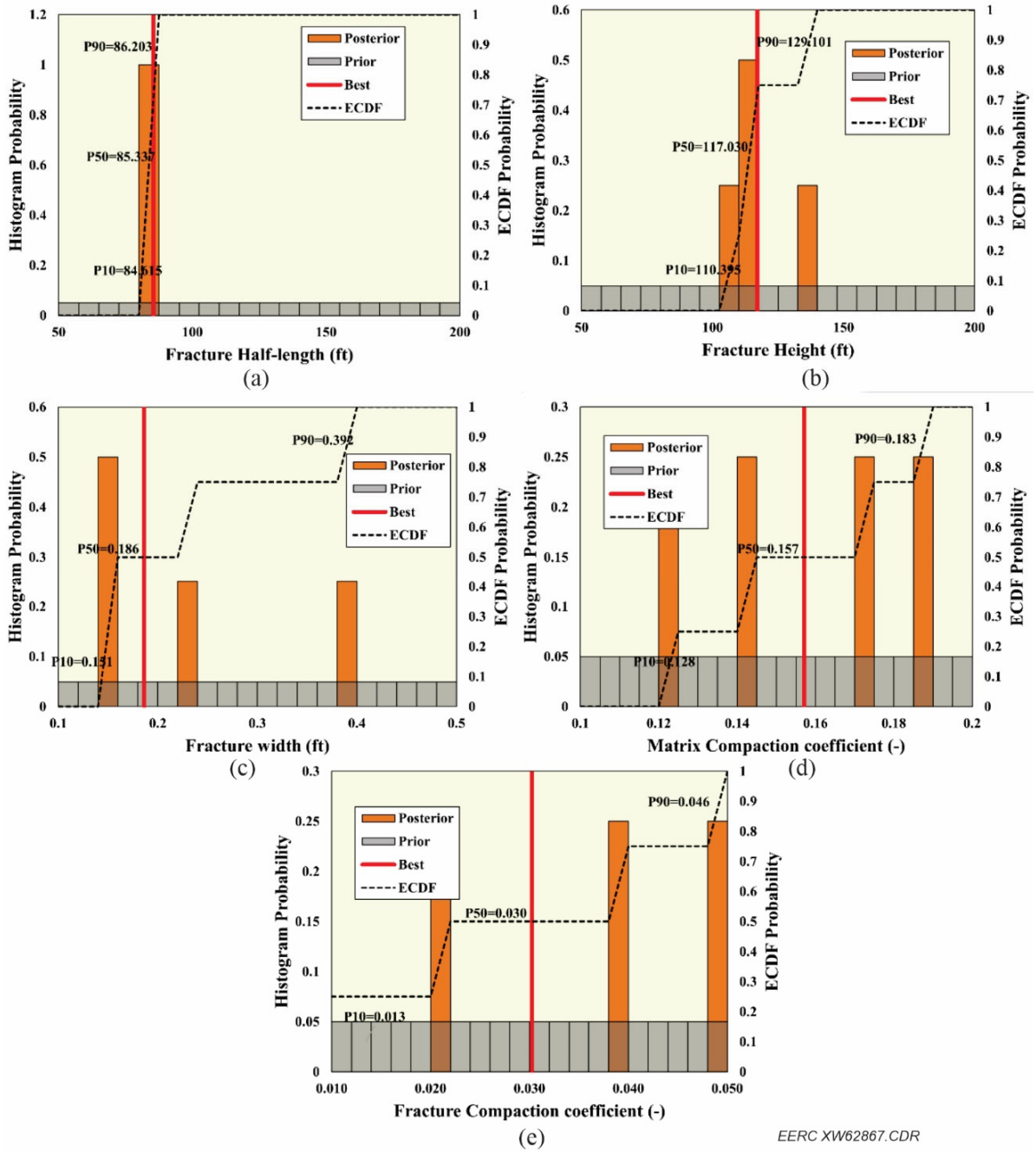


Figure A9. Prior and posterior distribution of uncertainty parameters for the four solutions of Scenario 10: (**a**) fracture half−length, (**b**) fracture height, (**c**) HF width, (**d**) matrix compaction coefficient, and (**e**) fracture compaction coefficient.

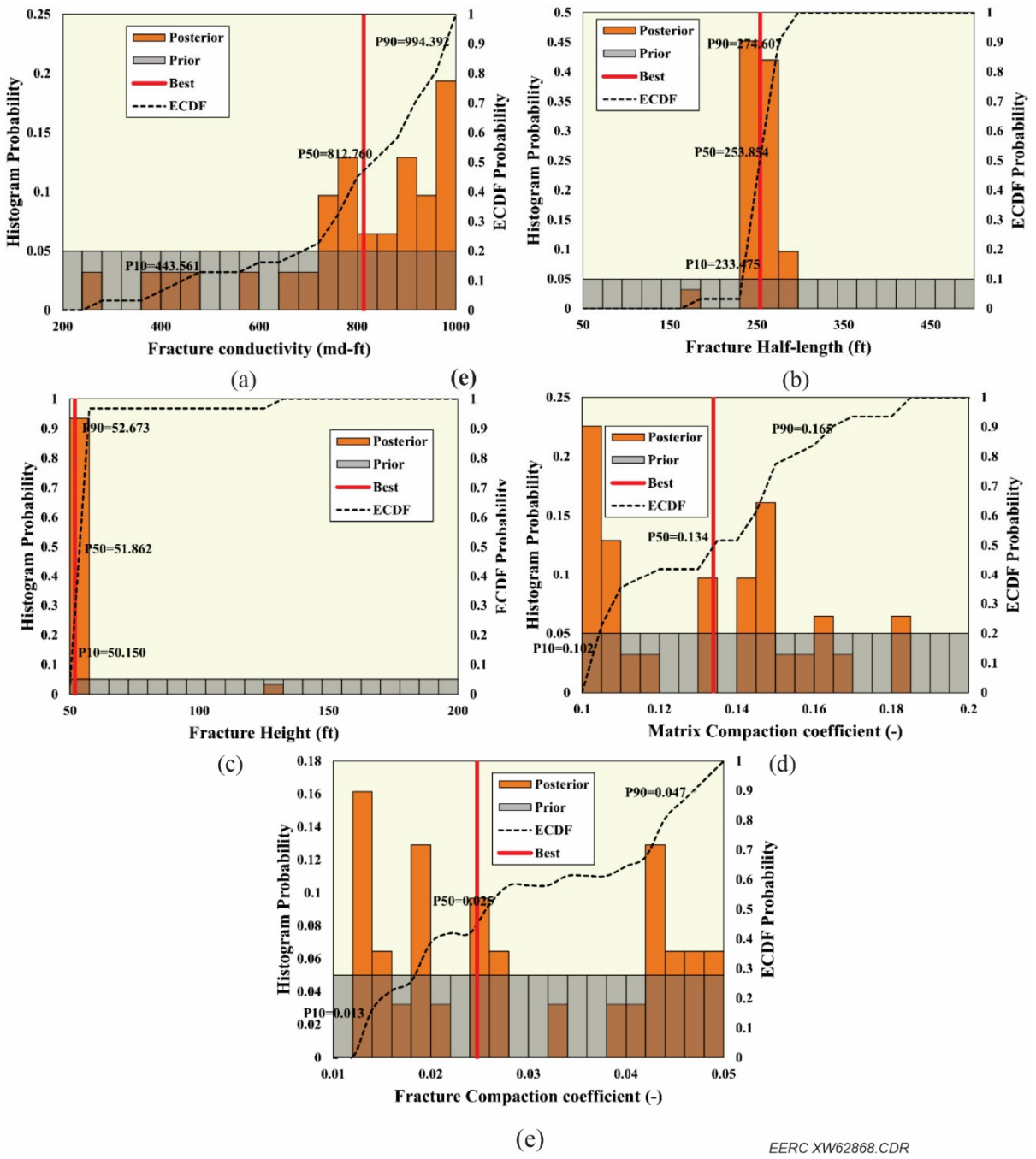


Figure A10. Prior and posterior distribution of uncertainty parameters for the 31 solutions of Scenario 11: (**a**) fracture conductivity, (**b**) fracture half−length, (**c**) fracture height, (**d**) matrix compaction coefficient, and (**e**) fracture compaction coefficient.

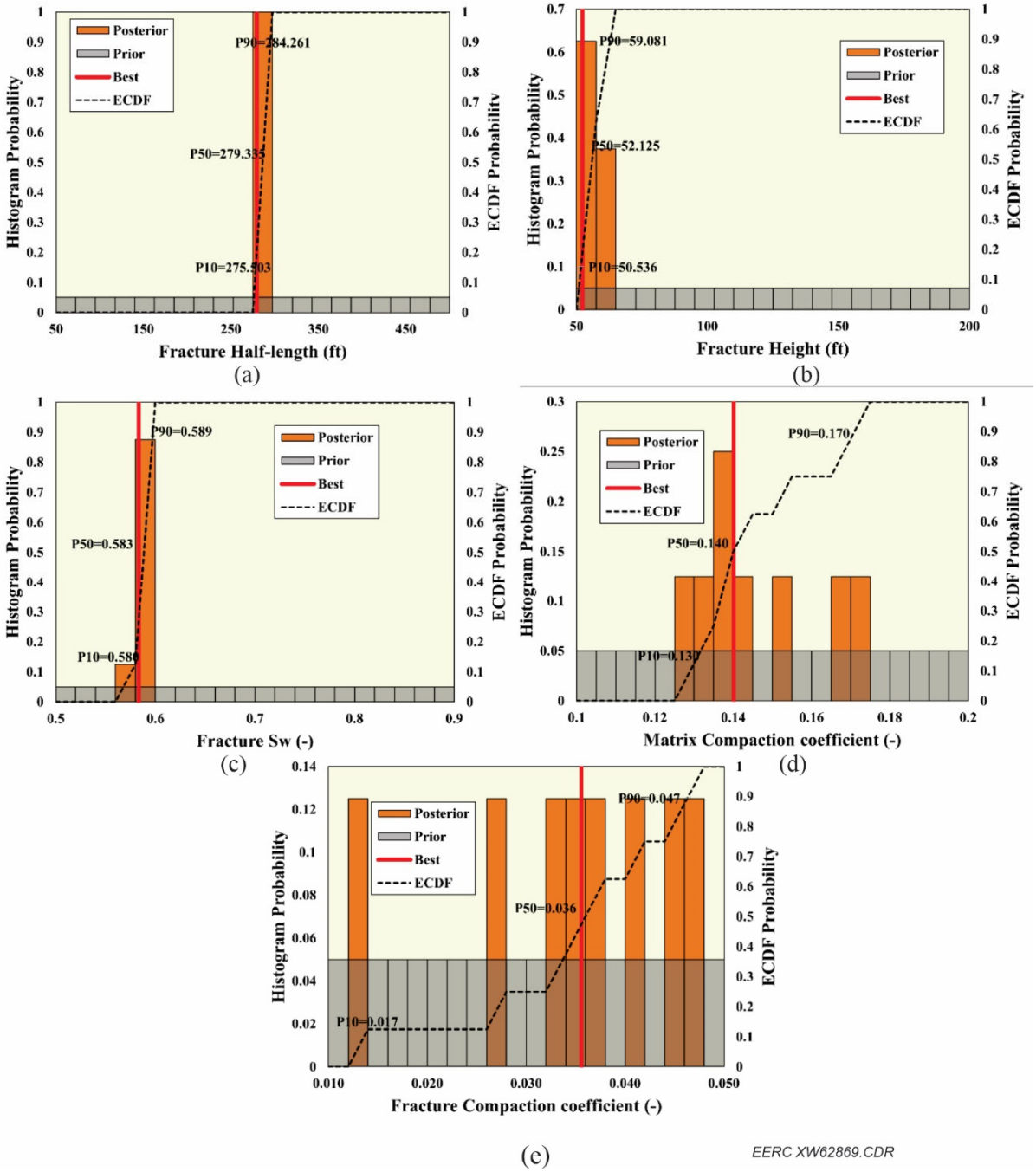


Figure A11. Prior and posterior distribution of uncertainty parameters for the eight solutions of Scenario 12: (**a**) fracture half−length, (**b**) fracture height, (**c**) fracture initial water saturation, (**d**) matrix compaction coefficient, and (**e**) fracture compaction coefficient.

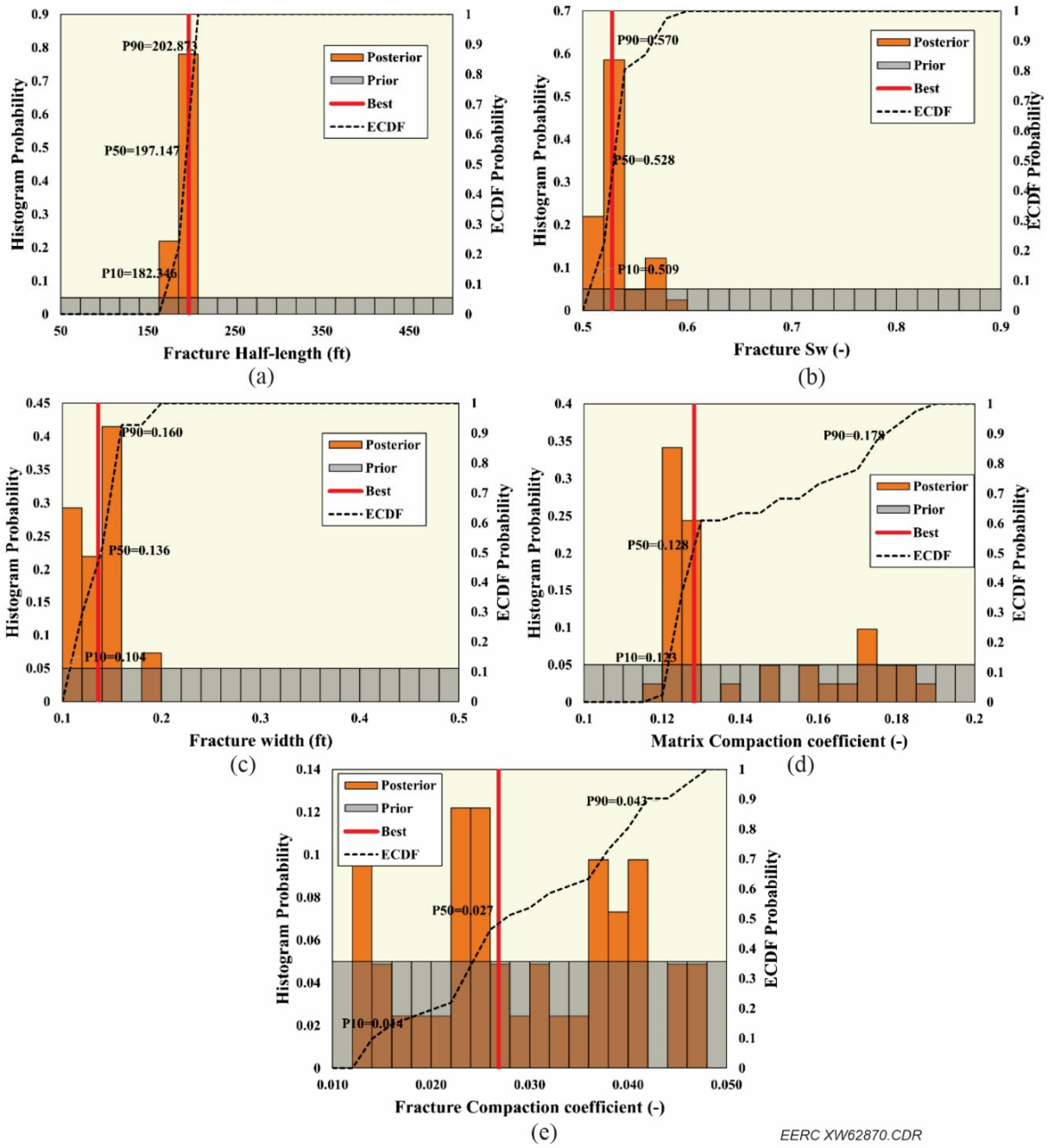


Figure A12. Prior and posterior distribution of uncertainty parameters for the 41 solutions of Scenario 13: (**a**) fracture half−length, (**b**) fracture initial water saturation, (**c**) fracture width, (**d**) matrix compaction coefficient, and (**e**) fracture compaction coefficient.

References

1. Li, L.; Su, Y.; Sheng, J.J.; Hao, Y.; Wang, W.; Lv, Y.; Zhao, Q.; Wang, H. Experimental and Numerical Study on CO_2 Sweep Volume during CO_2 Huff-n-Puff Enhanced Oil Recovery Process in Shale Oil Reservoirs. *Energy Fuels* **2019**, *33*, 4017–4032. [CrossRef]
2. Cipolla, C.; Wallace, J. Stimulated Reservoir Volume: A Misapplied Concept? In Proceedings of the SPE Hydraulic Fracturing Technology Conference, The Woodlands, TX, USA, 4–6 February 2014. [CrossRef]
3. Oliver, D.S.; Chen, Y. Recent Progress on Reservoir History Matching: A review. *Comput. Geosci.* **2011**, *15*, 185–221. [CrossRef]
4. Liu, N.; Oliver, D.S. Evaluation of Monte Carlo Methods for Assessing Uncertainty. *SPE J.* **2003**, *8*, 188–195. [CrossRef]
5. Emerick, A.A.; Reynolds, A.C. Investigation of the Sampling Performance of Ensemble-Based Methods with a Simple Reservoir Model. *Comput. Geosci.* **2013**, *17*, 325–350. [CrossRef]

6. Reynolds, A.C.; He, N.; Oliver, D.S. Reducing Uncertainty in Geostatistical Description with Well Testing Pressure Data. In *Reservoir Characterization—Recent Advances*; Schatzinger, R.A., Jordan, J.F., Eds.; AAPG: Tulsa, OK, USA, 1999; Volume 71, pp. 149–162.
7. Chen, C.; Gao, G.; Li, R.; Cao, R.; Chen, T.; Vink, J.C.; Gelderblom, P. Global-Search Distributed-Gauss-Newton Optimization Method and Its Integration with the Randomized-Maximum-Likelihood Method for Uncertainty Quantification of Reservoir Performance. *SPE J.* **2018**, *23*, 1496–1517. [CrossRef]
8. Oliver, D.S. Metropolized Randomized Maximum Likelihood for Sampling from Multimodal Distributions. *arXiv* **2015**, arXiv:1507.08563. [CrossRef]
9. Maschio, C.; Schiozer, D.J. Bayesian History Matching Using Artificial Neural Network and Markov Chain Monte Carlo. *J. Pet. Sci. Eng.* **2014**, *123*, 62–71. [CrossRef]
10. Tripoppoom, S.; Wang, X.; Liu, Z.; Yu, W.; Xie, H.; Sepehrnoori, K.; Miao, J. Characterizing Hydraulic and Natural Fractures Properties in Shale Oil Well in Permian Basin Using Assisted History Matching. *Fuel* **2020**, *275*, 117950. [CrossRef]
11. Warren, J.E.; Root, P.J. The Behavior of Naturally Fractured Reservoirs. *SPE J.* **1963**, *3*, 245–255. [CrossRef]
12. Yu, W.; Javadpour, F.; Varavei, A.; Sepehrnoori, K. Sensitivity Analysis of Hydraulic Fracture Geometry in Shale Gas Reservoirs. *SPE J.* **2014**, *113*, 1–7. [CrossRef]
13. Jiang, J.; Rami, M.Y. Hybrid Coupled Discrete-Fracture/Matrix and Multicontinuum Models for Unconventional-Reservoir Simulation. *SPE J.* **2016**, *21*, 1009–1027. [CrossRef]
14. Choi, E.S.; Cheema, T.; Islam, M.R. A New Dual-Porosity/Dual-Permeability Model with Non-Darcian Flow through Fractures. *J. Pet. Sci. Eng.* **1997**, *17*, 331–344. [CrossRef]
15. Conlin, J.M.; Hale, J.L.; Sabathier, J.C.; Faure, F.; Mas, D. Multiple-Fracture Horizontal Wells—Performance and Numerical Simulation. In Proceedings of the European Petroleum Conference, The Hague, The Netherlands, 19–21 September 1990. [CrossRef]
16. Mirzaei, M.; Cipolla, C.L. A Workflow for Modeling and Simulation of Hydraulic Fractures in Unconventional Gas Reservoirs. In Proceedings of the SPE Middle East Unconventional Gas Conference and Exhibition, Abu Dhabi, United Arab Emirates, 23–25 March 2012. [CrossRef]
17. U.S. Energy Information Administration. Petroleum & Other Liquids. 2022. Available online: www.eia.gov/petroleum/ (accessed on 22 August 2022).
18. Gaswirth, S.B.; Marra, K.R.; Lillis, P.G.; Mercier, T.J.; Leathers-Miller, H.M.; Schenk, C.J.; Klett, T.R.; Le, P.A.; Tennyson, M.E.; Hawkins, S.J.; et al. Assessment of Undiscovered Continuous Oil Resources in the Wolfcamp Shale of the Midland Basin, Permian Basin Province, Texas. In *U.S. Geological Survey Fact Sheet 2016–3092*; U.S. Geological Survey: Reston, VA, USA, 2016. [CrossRef]
19. Handford, C.R.; Loucks, R.G. Chapter 1. Responses of Carbonate Platforms to Relative Sea-Level Changes. In *Carbonate Sequence Stratigraphy: Recent Developments and Applications*; American Association of Petroleum Geologists: Tulsa, OK, USA, 1993; pp. 3–41. [CrossRef]
20. Meissner, F.G. Cyclic Sedimentation in Middle Permian Strata of the Permian Basin. In *Cyclic Sedimentation in the Permian Basin*; Elam, J.G., Chuber, S., Eds.; West Texas Geological Society: Midland, TX, USA, 1972; pp. 203–232.
21. Baldwin, P.W. Lithostratigraphic and Geochemical Characterization of the Upper Pennsylvanian Wolfcamp D Shale, Midland Basin (USA): Implications for the Paleoenvironments and Unconventional Petroleum Reservoirs. Theses and Dissertations—Earth and Environmental Sciences. 2016. Available online: https://uknowledge.uky.edu/ees_etds/35 (accessed on 1 November 2022). [CrossRef]
22. Hackley, P.C.; Zhang, T.; Jubb, A.M.; Valentine, B.J.; Dulong, F.T.; Hatcherian, J.J. Organic Petrography of Leonardian (Wolfcamp A) Mudrocks and Carbonates, Midland Basin, Texas: The Fate of Oil-Prone Sedimentary Organic Matter in the Oil Window. *Mar. Petrol. Geol.* **2020**, *112*, 104086. [CrossRef]
23. Li, T.; Chu, W.; Leonard, P.A. Analysis and Interpretations of Pressure Data from the Hydraulic Fracturing Test Site (HFTS). In Proceedings of the SPE/AAPG/SEG Unconventional Resources Technology Conference, Denver, CO, USA, 22–24 July 2019.
24. Courtier, J.; Gray, D.; Smith, M.; Stegent, N.; Carmichael, J.; Hassan, M.; Ciezobka, J. Legacy Well Protection Refrac Mitigates Offset Well Completion Communications in Joint Industry Project. In Proceedings of the SPE Liquids-Rich Basins Conference–North America, Midland, TX, USA, 21–22 September 2016. [CrossRef]
25. Stegent, N.; Candler, C. Downhole Microseismic Mapping of More Than 400 Fracturing Stages on a Multiwell Pad at the Hydraulic Fracturing Test Site (HFTS): Discussion of Operational Challenges and Analytic Results. In Proceedings of the SPE/AAPG/SEG Unconventional Resources Technology Conference, Houston, TX, USA, 23–25 July 2018. [CrossRef]
26. Gale, J.; Elliott, S.; Li, J.Z.; Laubach, S. Natural Fracture Characterization in the Wolfcamp Formation at the Hydraulic Fracture Test Site (HFTS), Midland Basin, Texas. In Proceedings of the SPE/AAPG/SEG Unconventional Resources Technology Conference, Denver, CO, USA, 22–24 July 2019.
27. Chow, V.T. On the Determination of Transmissibility and Storage Coefficients from Pumping Test Data. *Trans. Am. Geophys. Union* **1952**, *33*, 397–404. [CrossRef]
28. Chu, C.; Pandya, N.D.; Flumerfelt, R.W.; Chen, C. Rate-Transient Analysis Based on the Power-Law Behavior for Permian Wells. *SPE Res. Eval. Eng.* **2019**, *22*, 1360–1370. [CrossRef]
29. Xu, Y. Implementation and Application of the Embedded Discrete Fracture Model (EDFM) for Reservoir Simulation in Fractured Reservoirs. Master's Thesis, The University of Texas at Austin, Austin, TX, USA, 2015.

30. Xu, Y.; Cavalcante Filho, J.S.A.; Yu, W.; Sepehrnoori, K. Discrete–fracture modeling of complex hydraulic–fracture geometries in reservoir simulators. *SPE Res. Eval. Eng.* **2017**, *20*, 403–422. [CrossRef]
31. Moinfar, A.; Varavei, A.; Sepehrnoori, K.; Johns, R.T. Development of a Coupled Dual Continuum and Discrete Fracture Model for the Simulation of Unconventional Reservoirs. In Proceedings of the SPE Reservoir Simulation Symposium, The Woodlands, TX, USA, 16–18 September 2013. [CrossRef]
32. Lee, S.H.; Lough, M.F.; Jensen, C.L. Hierarchical Modeling of Flow in Naturally Fractured Formations with Multiple Length Scales. *Water Resour. Res.* **2001**, *37*, 443–455. [CrossRef]
33. Li, L.; Lee, S.H. Efficient Field–Scale Simulation of Black Oil in a Naturally Fractured Reservoir through Discrete Fracture Networks and Homogenized Media. *SPE Res. Eval. Eng.* **2008**, *11*, 750–758. [CrossRef]
34. Wan, X.; Rasouli, V.; Damjanac, B.; Yu, W.; Xie, H.; Li, N.; Rabiei, M.; Miao, J.; Liu, M. Coupling of Fracture Model with Reservoir Simulation to Simulate Shale Gas Production with Complex Fractures and Nanopores. *J. Pet. Sci. Eng.* **2020**, *193*, 107422. [CrossRef]
35. Weijermars, R.; Nandlal, K.; Tugan, M.F.; Dusterhoft, R.; Stegent, N. Wolfcamp Hydraulic Fracture Test Site Drained Rock Volume and Recovery Factors Visualized by Scaled Complex Analysis Method (CAM): Emulating Multiple Data Sources (production rates, water cuts, pressure gauges, flow regime changes, and b-sigmoids). In Proceedings of the Unconventional Resources Technology Conference, Online, 20–22 July 2020.
36. SimTech, L.L.C. EDFM-AI Automatic History Matching (AHM). Available online: www.simtechnologyus.com/ahm.html (accessed on 1 November 2022).
37. Carpenter, C. Embedded Discrete Fracture Modeling with Artificial Intelligence in Permian Basin. *JPT* **2018**, *70*, 63–64. [CrossRef]
38. Dachanuwattana, S.; Xia, Z.; Yu, W.; Qu, L.; Wang, P.; Liu, W.; Miao, J.; Sepehrnoori, K. Application of Proxy-Based MCMC and EDFM to History Match a Shale Gas Condensate Well. *J. Pet. Sci. Eng.* **2018**, *167*, 486–497. [CrossRef]
39. Dachanuwattana, S.; Yu, W.; Sepehrnoori, K. An Efficient MCMC History Matching Workflow Using Fit-for-Purpose Proxies Applied in Unconventional Oil Reservoirs. *J. Pet. Sci. Eng.* **2019**, *176*, 381–395. [CrossRef]
40. Eltahan, E.; Yu, W.; Sepehrnoori, K.; Kerr, E.; Miao, J.; Ambrose, R. Modeling Naturally and Hydraulically Fractured Reservoirs with Artificial Intelligence and Assisted History Matching Methods Using Physics-Based Simulators. In Proceedings of the SPE Western Regional Meeting, San Jose, CA, USA, 23–26 April 2019. [CrossRef]
41. Eltahan, E.; Ganjdanesh, R.; Yu, W.; Sepehrnoori, K.; Drozd, H.; Ambrose, R. Assisted history matching using Bayesian inference: Application to Multi-Well Simulation of a Huff-N-Puff Pilot Test in the Permian Basin. In Proceedings of the SPE/AAPG/SEG Unconventional Resources Technology Conference, Online, 20–22 July 2020. [CrossRef]
42. Tripoppoom, S.; Yu, W.; Huang, H.; Sepehrnoori, K.; Song, W.; Dachanuwattana, S. A Practical and Efficient Iterative History Matching Workflow for Shale Gas Well Coupling Multiple Objective Functions, Multiple Proxy-Based MCMC and EDFM. *J. Pet. Sci. Eng.* **2019**, *176*, 594–611. [CrossRef]
43. Tripoppoom, S.; Xie, J.; Yong, R.; Wu, J.; Yu, W.; Sepehrnoori, K.; Miao, J.; Chang, C.; Li, N. Investigation of Different Production Performances in Shale Gas Wells Using Assisted History Matching: Hydraulic Fractures and Reservoir Characterization from Production Data. *Fuel* **2020**, *267*, 117097. [CrossRef]
44. Du, S.; Liang, B.; Yuanbo, L. Field study: Embedded Discrete Fracture Modeling with Artificial Intelligence in Permian Basin for Shale Formation. In Proceedings of the SPE Annual Technical Conference and Exhibition, San Antonio, TX, USA, 9–11 October 2017. [CrossRef]
45. Liu, C. Automatic History Matching with Data Integration for Unconventional Reservoirs. Master's Thesis, The University of Texas at Austin, Austin, TX, USA, 2021.
46. McKay, M.D.; Beckman, R.J.; Conover, W.J. A Comparison of Three Methods for Selecting Values of Input Variables in the Analysis of Output from a Computer Code. *Technometrics* **1979**, *21*, 239–245.
47. Liu, C.; Yu, W.; Chang, C.; Li, Q.; Sepehrnoori, K. Proxy based Assisted History Matching and Well Spacing Optimization in Shale Gas Development of a Real Field Case. In Proceedings of the SPE Improved Oil Recovery Conference, Online, 31 August–4 September 2020. [CrossRef]
48. Johns, R.T.; Sah, P.; Solano, R. Effect of Dispersion on Local Displacement Efficiency for Multicomponent Enriched-Gas Floods Above the Minimum Miscibility Enrichment. *SPE Res. Eval. Eng.* **2002**, *5*, 4–10. [CrossRef]
49. Shtepani, E. Experimental and Modeling Requirements for Compositional Simulation of Miscible CO_2-EOR Processes. In Proceedings of the SPE/EAGE Reservoir Characterization and Simulation Conference, Abu Dhabi, United Arab Emirates, 28–31 October 2007. [CrossRef]
50. Tovar, F.D.; Barrufet, M.A.; Schechter, D.S. Enhanced Oil Recovery in the Wolfcamp Shale by Carbon Dioxide or Nitrogen Injection: An Experimental Investigation. *SPE J.* **2021**, *26*, 515–537. [CrossRef]
51. Burrows, L.C.; Haeri, F.; Cvetic, P.; Sanguinito, S.; Shi, F.; Tapriyal, D.; Goodman, A.; Enick, R.M. A Literature Review of CO_2, Natural Gas, and Water-Based Fluids for Enhanced Oil Recovery in Unconventional Reservoirs. *Energy Fuels* **2020**, *34*, 5331–5380. [CrossRef]
52. Hawthorne, S.B.; Miller, D.J.; Jin, L.; Gorecki, C.D. Rapid and Simple Capillary-Rise/Vanishing Interfacial Tension Method to Determine Crude Oil Minimum Miscibility Pressure—Pure and Mixed CO_2, Methane, and Ethane. *Energy Fuels* **2016**, *30*, 6365–6372. [CrossRef]

53. Jin, L.; Pekot, L.J.; Hawthorne, S.B.; Salako, O.; Peterson, K.J.; Bosshart, N.W.; Jiang, T.; Hamling, J.A.; Gorecki, C.D. Evaluation of Recycle Gas Injection on CO_2 Enhanced Oil Recovery and Associated Storage Performance. *Int. J. Greenh. Gas Control* **2018**, *75*, 151–161. [CrossRef]
54. Jin, L.; Pekot, L.J.; Smith, S.A.; Salako, O.; Peterson, K.J.; Bosshart, N.W.; Hamling, J.A.; Mibeck, B.A.; Hurley, J.P.; Beddoe, C.J.; et al. Effects of Gas Relative Permeability Hysteresis and Solubility on Associated CO_2 Storage Performance. *Int. J. Greenh. Gas Control* **2018**, *75*, 140–150. [CrossRef]
55. Hawthorne, S.B.; Miller, D.J.; Grabanski, C.B.; Sorensen, J.A.; Pekot, L.J.; Kurz, B.A.; Gorecki, C.D.; Steadman, E.N.; Harju, J.A.; Melzer, S. Measured Crude Oil MMPs with Pure and Mixed CO_2, Methane, and Ethane, and Their Relevance to Enhanced Oil Recovery from Middle Bakken and Bakken Shales. In Proceedings of the SPE Unconventional Resources Conference, Calgary, AB, Canada, 15–16 February 2017. [CrossRef]
56. Adel, I.A.; Tovar, F.D.; Zhang, F.; Schechter, D.S. The Impact of MMP on Recovery Factor During CO_2–EOR in Unconventional Liquid Reservoirs. In Proceedings of the SPE Annual Technical Conference and Exhibition, Dallas, TX, USA, 24–26 September 2018. [CrossRef]
57. Li, L.; Zhang, Y.; Sheng, J.J. Effect of the Injection Pressure on Enhancing Oil Recovery in Shale Cores during the CO_2 Huff-n-Puff Process When It Is above and below the Minimum Miscibility Pressure. *Energy Fuels* **2017**, *31*, 3856–3867. [CrossRef]
58. Salman, M.; Kostarelos, K.; Sharma, P.; Lee, J.H. Application of Miscible Ethane Foam for Gas EOR Conformance in Low-Permeability Heterogeneous Harsh Environments. *SPE J.* **2020**, *25*, 1871–1883. [CrossRef]
59. Balasubramanian, S.; Chen, P.; Bose, S.; Alzahabi, A.; Thakur, G.C. Recent Advances in Enhanced Oil Recovery Technologies for Unconventional Oil Reservoirs. In Proceedings of the Offshore Technology Conference, Houston, TX, USA, 30 April–3 May 2018.